Chem Soc Rev

Dynamic Article Links

Cite this: *Chem. Soc. Rev.*, 2011, **40**, 1059–1080

www.rsc.org/csr

CRITICAL REVIEW

Mechanical properties of hybrid inorganic–organic framework materials: establishing fundamental structure–property relationships†

Jin Chong Tan and Anthony K. Cheetham*

Received 2nd November 2010
DOI: 10.1039/c0cs00163e

The mechanical properties of hybrid framework materials, including both nanoporous metal–organic frameworks (MOFs) and dense inorganic–organic frameworks, are discussed in this *critical review*. Although there are relatively few studies of this kind in the literature, major recent advances in this area are beginning to shed light on the fundamental structure–mechanical property relationships. Indeed research into the mechanical behavior of this important new class of solid-state materials is central to the design and optimal performance of a multitude of technological applications envisaged. In this review, we examine the elasticity of hybrid frameworks by considering their Young's modulus, Poisson's ratio, bulk modulus and shear modulus. This is followed by discussions of their hardness, plasticity, yield strength and fracture behavior. Our focus is on both experimental and computational approaches. Experimental work on single crystals and amorphized monoliths involved primarily the application of nanoindentation and atomic force microscopy to determine the elastic moduli and hardness properties. The compressibility and bulk moduli of single crystals and polycrystalline powders were studied by high-pressure X-ray crystallography in the diamond anvil cell, while in one instance spectroscopic ellipsometry has also been used to estimate the elastic moduli of MOF nanoparticles and deposited films. Theoretical studies, on the other hand, encompassed the application of first principles density-functional calculations and finite-temperature molecular dynamics simulations. Finally, by virtue of the diverse mechanical properties achievable in hybrid framework materials, we propose that a new domain be established in the materials selection map to define this emerging class of materials (137 references).

1. Introduction

The field of hybrid inorganic–organic framework materials now represents one of the fastest growing areas in materials chemistry because their enormous structural and chemical diversity presents vast opportunities for creating many technologically relevant properties.[1] One exciting opportunity arises from creating hybrid framework materials that have properties similar to those of classical inorganic materials, but with much lower densities characteristic of organic systems. Another lies in designing hybrid materials that exhibit the functionality of organic materials, but with superior thermal stability characteristic of inorganic systems. Indeed, there is a huge scope for creating unusual properties or unique combinations of properties that are not possible in purely inorganic or organic systems alone.[2]

Hybrid framework materials are defined as single-phase crystalline compounds encompassing both inorganic and organic moieties as integral parts of a network with infinite bonding connectivity in at least one dimension.[1] Importantly, such hybrid systems are held together by strong covalent and/or coordination bonding to afford one-dimensional (1-D) chains, 2-D layers, or 3-D networks that may incorporate organic and/or inorganic connectivities. In this context, hybrid inorganic–organic framework materials (herein referred to as hybrid frameworks) are not to be confused with hybrid nanocomposite systems, in which their organic and inorganic components exist as distinct and separate phases (*e.g.* carbon nanotube-inorganic hybrids[3]). Consequently, we shall not attempt to cover the extensive work on the mechanical properties of nanocomposite materials.[4–6] Hybrid frameworks also exclude molecular and oligomeric systems that form networks through weak non-covalent interactions (*e.g.* hybrid supramolecular assemblies[7]). Likewise, systems for which the organic component is present only as a guest entity occupying the cavity of an inorganic framework are not considered as hybrid frameworks (*e.g.* aluminosilicate zeolites hosting guests molecules[8]).

Department of Materials Science and Metallurgy, University of Cambridge, Pembroke Street, Cambridge CB2 3QZ, UK. E-mail: akc30@cam.ac.uk; Fax: +44 1223 334567; Tel: +44 1223 767061

† Part of the themed issue on hybrid materials.

There have been several excellent reviews on the structure and properties of inorganic–organic framework materials.[9–13] The classification, structural diversity and chemical trends of hybrid frameworks have been covered in detail in a recent article by Cheetham *et al.*[1] For the purpose of this review, there are two broad categories of hybrid inorganic–organic frameworks. (i) Nanoporous hybrid frameworks—commonly called metal–organic frameworks (MOFs)—are attracting considerable attention by virtue of their exceptionally high porosity (nano-scale pore size between 0.4–6 nm) in combination with their highly tuneable structural architecture and chemical functionality.[10,11,14] Over the past decade, a huge body of research has focused on the reticular design and synthesis of MOFs, aimed at gas storage,[15,16] molecular separation,[17] catalysis,[18,19] drug delivery,[20,21] and sensing applications.[22] (ii) Dense hybrid frameworks incorporate infinite inorganic connectivity, especially those based on metal–oxygen–metal (M–O–M) arrays. Notably, their structures closely resemble those of classical inorganic materials. There is now a rapidly growing literature on dense hybrids shown to exhibit attractive physical phenomena traditionally associated only with purely inorganic or organic materials; these include electrical, magnetic, optical and multiferroic properties.[2,23,24]

In contrast to the sheer number of recent publications dealing with the synthesis of novel framework structures and characterization of their functional properties, studies devoted to understanding the mechanical properties of hybrid frameworks are comparatively few. The aim of this critical review is thus to bridge this gap by highlighting the recent advances with a view to stimulate further research in this important field. Undoubtedly, the structural robustness and resilience of hybrid frameworks under (static or dynamic) mechanical stresses are central to the optimal performance of the envisaged technological applications.

Depending on the proposed application (Fig. 1), the mechanical loading can act in tension, compression, shear, bending, torsion, impact or indeed any combinations of the above; and in some cases coupled with cyclic thermo-mechanical effects. By way of an example, MOFs put under hydrostatic compression in gas sorption applications must exhibit good mechanical stability (*e.g.* high bulk and shear moduli) to avert excessive structural distortion, framework collapse and even pressure-induced amorphization.[25] In relation to stress-induced chemical sensing devices based on thin-film MOF structures (*e.g.* micro-cantilevers integrated with thin films of Cu-BTC (HKUST-1)[26]), the film stiffness (*i.e.* its Young's modulus) and the film-to-substrate adhesion strength are key mechanical properties to be addressed to control irreversible plastic deformation and shear delamination failures, among others. In addition, the performance of piezoelectric devices such as actuators and sensors is strongly dependent upon the elastic properties of the underlying framework structure to afford effective electro–mechanical energy conversion. Another exemplar concerns MOF coatings or membranes[27–29]

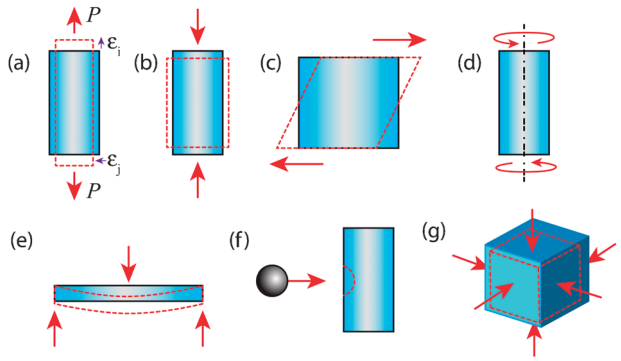

Fig. 1 An illustration depicting the common modes of mechanical loading: (a) uniaxial tension, where ε_i and ε_j (strain, ε = extension/original length) denote the axial and the lateral strains respectively, as resulted by the external load *P*, (b) uniaxial compression, (c) shear, (d) torsion, (e) bending, (f) impact, and (g) hydrostatic compression. Red dotted lines are used to delineate the distorted geometries.

Jin Chong Tan

Jin-Chong Tan is a Post-doctoral Research Fellow in the Department of Materials Science & Metallurgy, Cambridge University. He obtained his PhD at Cambridge (2005) in the field of highly porous composite systems and coatings, under the supervision of Prof. T. W. Clyne. Between 2006 and 2010, he was a Junior Research Fellow in Materials Science at Wolfson College, Cambridge. In 2008, he joined the group of Prof. A. K. Cheetham to work on the micro-/nano-mechanical characterization of hybrid framework materials using nanoindentation and atomic force microscopy. His current research interests focus on metal–organic frameworks and advanced coatings for structural and functional applications.

Anthony K. Cheetham

Tony Cheetham obtained his DPhil at Oxford in 1971 and did post-doctoral work in the Materials Physics Division at Harwell. He joined the Chemistry Faculty at Oxford in 1974, and then moved to the University of California at Santa Barbara in 1991 to become Professor in the Materials Department and Director of the newly-created Materials Research Laboratory. He was also the founding Director of the International Center for Materials Research at UCSB (2004). Cheetham moved to Cambridge in 2007 to take up the Goldsmiths' Chair of Materials Science. He is a Fellow of the Royal Society (1994) and several other academies, and has received numerous international awards for his work in the field of materials chemistry.

intended for catalytic applications; such thin structures have to have sufficiently high thermo-mechanical stability and fracture toughness to endure stresses generated by a combination of intense fluxes and large thermal gradients.

Since 2006, partly motivated by their rapid developments toward practical applications, a number of studies concerning the mechanical behavior of hybrid framework materials have started to emerge. In this respect, the relatively few published works hitherto are limited to the following: (i) Dense hybrid frameworks—copper phosphonoacetate; CuPA [$Cu_{1.5}(H_2O)(O_3PCH_2CO_2)$],[30] cerium oxalate formate [$Ce(C_2O_4)(HCO_2)$],[31] and zinc phosphate phosphonoacetate; ZnPA [$Zn_3(H_2O)(PO_4)(O_2CCH_2PO_3)$].[32] (ii) Nanoporous hybrid frameworks (MOFs)—Isoreticular MOFs (IRMOFs) including MOF-5 [$ZnO_4(BDC)_3$],[33–39] Cu-BTC or HKUST-1 [$Cu_3(BTC)_2$],[40–42] Zeolitic Imidazolate Frameworks; ZIFs [$Zn(Im)_2$ and structures with substituted imidazoles],[25,43–45] lithium boron imidazolate; BIF-1-Li [$LiB(Im)_4$],[46] and MIL-101(Cr) [$Cr_3F(H_2O)_2O(BDC)_3$].[47]

In this review, we will focus on key findings pertaining to the mechanical properties of both dense and nanoporous hybrid framework materials; their elasticity, hardness, plasticity, yield strength, and fracture toughness characteristics will be discussed in turn. But before we begin, to serve as an overview—let us consider their elastic modulus (E) and hardness (H) experimental data represented as a materials selection map alongside other major categories of "conventional" materials (Fig. 2). To provide the reader with a more comprehensive picture, we have also incorporated our most recently acquired data.[48] It is particularly striking to see that the dense and the nanoporous hybrid frameworks populate two very distinctive regions in the chart, and to some extent straddle the border between polymeric (purely organic), ceramic (purely inorganic) and metallic materials. In light of this, we wish to propose a new domain to be associated with hybrid frameworks as denoted by the dotted lines in Fig. 2. Specifically, in view of their vast chemical and structural diversity,[1] we anticipate that the mechanical properties of this new family of materials can potentially be tailored and improved *via* a "bottom-up" crystal engineering approach[49,50] to meet the requirements of specific applications.

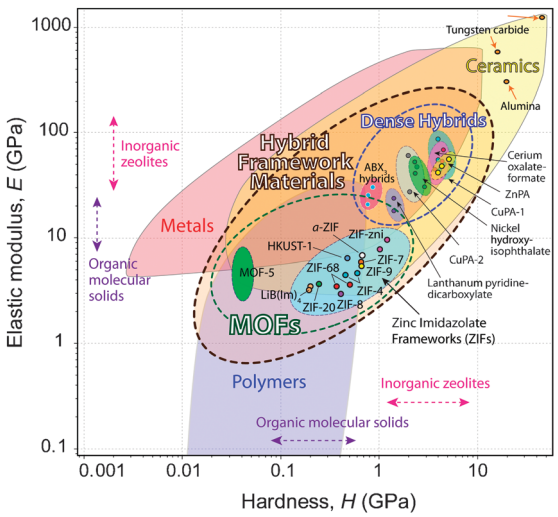

Fig. 2 Elastic modulus *versus* hardness materials property map for hybrid framework materials, encompassing both dense and nanoporous (MOFs) framework structures presented with other major classes of materials. Experimental data collected from published sources: CuPA-1 and CuPA-2 polymorphs,[30] cerium oxalate formate,[31] ZnPA,[32] ZIFs,[44] *a*-ZIF,[45] $LiB(Im)_4$,[46] MOF-5.[36] Unpublished data of hybrids include: HKUST-1, nickel hydroxyisophthalate, lanthanum pyridinedicarboxylate, and hybrids with ABX_3 perovskite architecture.[48] Examples of purely organic molecular crystals studied by nanoindentation include (i) MTN [2-(methylthio)nicotinic acid][122] with $E \approx 15$ GPa; $H \approx 0.2$–0.4 GPa, and (ii) saccharin [$C_7H_5NO_3S$][123] with $E \approx 13$–14 GPa; $H \approx 0.5$–0.6 GPa. Representative experimental data of inorganic zeolites single crystals: ZSM-5 ($E \approx 57$ GPa; $H \approx 7$ GPa),[124] Silicalite-1 ($E \approx 40$ GPa; $H \approx 2.5$ GPa),[125] Analcime ($E = 96$ GPa),[126] and Natrolite ($E \approx 78$ GPa).[97]

2. Elasticity

We start by examining the mechanical response of hybrid framework materials when subjected to low loads (below the material yield strength) thus resulting in small reversible deformations or elastic strains. Our discussion will focus on examples reported to date, which mainly concern the Young's modulus (E) and the bulk modulus (K) determined from experimental methods (nanoindentation, high-pressure crystallography, atomic force microscopy and spectroscopic ellipsometry) and computational techniques (density-functional theory (DFT) and molecular dynamics (MD)). The objective is to understand the elasticity of hybrid frameworks in terms of their underlying structural dimensionality, framework density, chemical topology and basic building blocks. On top of that, some information relating to their shear modulus (G) and the Poisson's ratio (ν) derived mainly from computer simulations are also presented.

2.1 Young's modulus and Poisson's ratio

In the context of hybrid framework materials, the Young's modulus (E) (or elastic modulus) is a measure of the stiffness of the framework structure under the effects of unidirectional loading (Fig. 1(a)–(b)), which tends to stretch or compress it elastically. Conversely, the reciprocal of the stiffness defines the compliance ($1/E$) of the framework. A framework structure deformed elastically and axially (*i.e.* along loading direction) will be accompanied by a lateral dimensional change; the ratio of the lateral strain ε_j to the axial strain ε_i is defined by the Poisson's ratio ($\nu = -\varepsilon_j/\varepsilon_i$), as illustrated in Fig. 1(a).

We note that most of the Young's modulus data presented here were obtained by nanoindentation, which is now a widely adopted nano-mechanical characterization technique[51] ideal for probing nanostructures, thin films, single crystals and small volumes of monoliths. The application of nanoindentation to anisotropic materials, however, requires some caution because the Oliver and Pharr method[52] for extracting the modulus data assumes an isotropic material response (true for non-textured polycrystalline materials). Also, given that the nature of the stress field developed under an indenter tip is not truly unidirectional, the Young's moduli measured this way could deviate from the intrinsic values.[53] Nevertheless, when

indenting low-symmetry single crystals, the measured modulus is strongly biased towards the intrinsic modulus along the indenter axis and can therefore provide a good first-order estimate of E.[54]

2.1.1 Dense hybrid frameworks

(a) Polymorphs of 2-D and 3-D frameworks. The first study on the elastic properties of dense hybrid frameworks concerned two low-symmetry polymorphs of copper phosphonoacetate (CuPA) frameworks: $Cu_{1.5}(H_2O)(O_3PCH_2CO_2)$.[30] The first polymorph, CuPA-1, is a three-dimensional framework (Fig. 3(a–b)) containing $Cu_3(H_2O)_2O_{10}$ trimers that are linked by two phosphonate units to form an unbroken chain of Cu–O–Cu–O–Cu–O–P–O–Cu linkages down the *a*-axis. These chains are cross-linked by phosphonate and carboxylate ligands to afford a dense 3-D framework. On the other hand, the second polymorph, CuPA-2, is a 2-D framework (Fig. 3(c–e)). It consists of 1-D metal–oxygen–metal (Cu–O–Cu) jagged chains lying along the *c*-direction, linked by phosphonoacetate groups to form 2-D layers that are hydrogen-bonded together. It is important to note that the layers are oriented almost perpendicular to the (100)-oriented facet, while being approximately parallel to (010).

The Young's moduli (E) of the single crystals were measured using a sharp-tipped Berkovich nanoindenter (3-sided pyramidal tip, end radius $\approx$50 nm) and the results (Fig. 4) reveal that the elastic anisotropy of CuPA can be directly correlated to the underlying crystal structures and framework dimensionalities. For CuPA-1, the (100)-oriented facet is the stiffest ($E_{(100)} \approx 93$ GPa), which is attributed to the stiff inorganic chains oriented along the *a*-axis. In contrast, the remaining low-index faces have relatively low moduli, with the ratio of $E_{(100)} : E_{(010)} : E_{(001)} : E_{(011)} = 1.86 : 1.09 : 1.00 : 1.15$; particularly because the loading direction (*i.e.* indenter axis) was directed approximately perpendicular to the inorganic linkages.

For CuPA-2 (Fig. 4(b)), in view of its layered architecture, both the (100)- and (001)-oriented facets are significantly stiffer when the loading direction is approximately parallel to the 2-D layers (61 GPa and 55 GPa respectively). Since the hydrogen-bonded layers are compliant when loaded in the normal orientation, the modulus of the (010)-oriented facet was measured to be up to 50% lower. This is expected as the strength of hydrogen bonding typically falls in the range of 5–65 kJ mol^{-1} that is comparable to van der Waals interaction (*ca.* 50 kJ mol^{-1}); but understandably a lot weaker than that of covalent ($\approx$350 kJ mol^{-1}) and most coordination bonding (50–200 kJ mol^{-1}).[55] Therefore in low-dimensional hybrid framework materials, especially those encompassing 1-D and 2-D structures, it is clear that combinations of strong covalent or coordination bonding coupled with weak intermolecular interactions (*e.g.* hydrogen bonding, π–π stacking, van der Waals) can produce frameworks with strongly anisotropic mechanical behavior.

Interestingly, the elastic anisotropy observed in CuPA-2 somewhat parallels that of graphite whose structure is also two-dimensional (Fig. 5). Even though the strong C–C bonds present in the basal planes of graphite (bond length 1.42 Å) can confer very high elastic stiffnesses, the weak van der Waals interactions between adjacent layers (interatomic distance

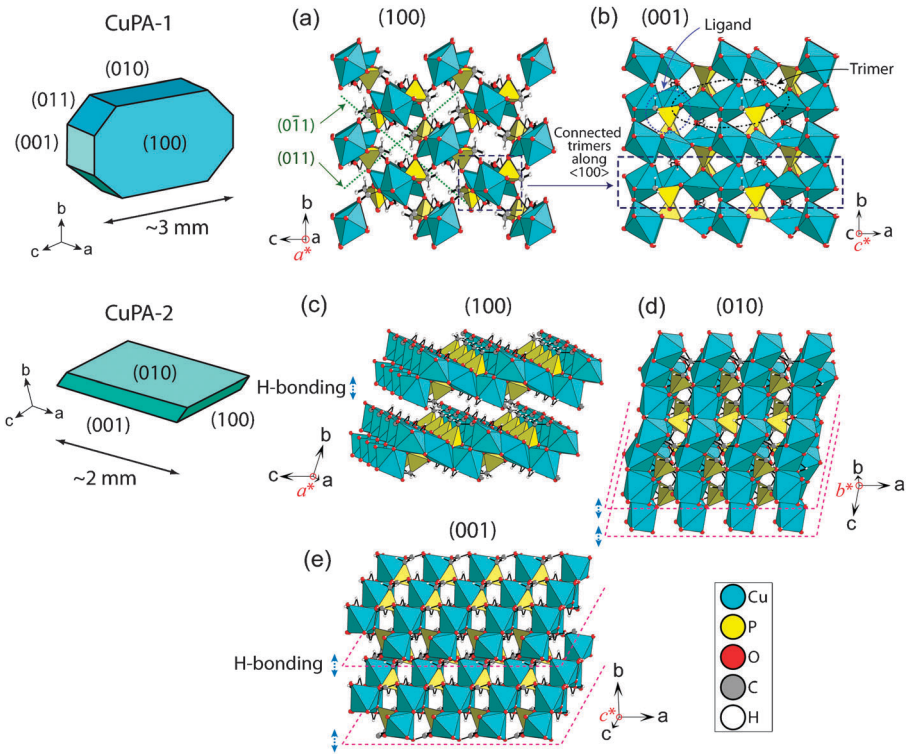

Fig. 3 Crystalline structures of CuPA-1 (monoclinic) and CuPA-2 (triclinic). (a)–(b) depict the CuPA-1 viewed perpendicular to the (100) and (001) planes respectively, *i.e.* normal to the nanoindenter axes. (c)–(e) Views of CuPA-2 perpendicular to the (100), (010) and (001) planes, respectively. Note that blue arrows denote the interlayer hydrogen bonds and red dotted lines highlight the layers. Adapted from ref. 30.

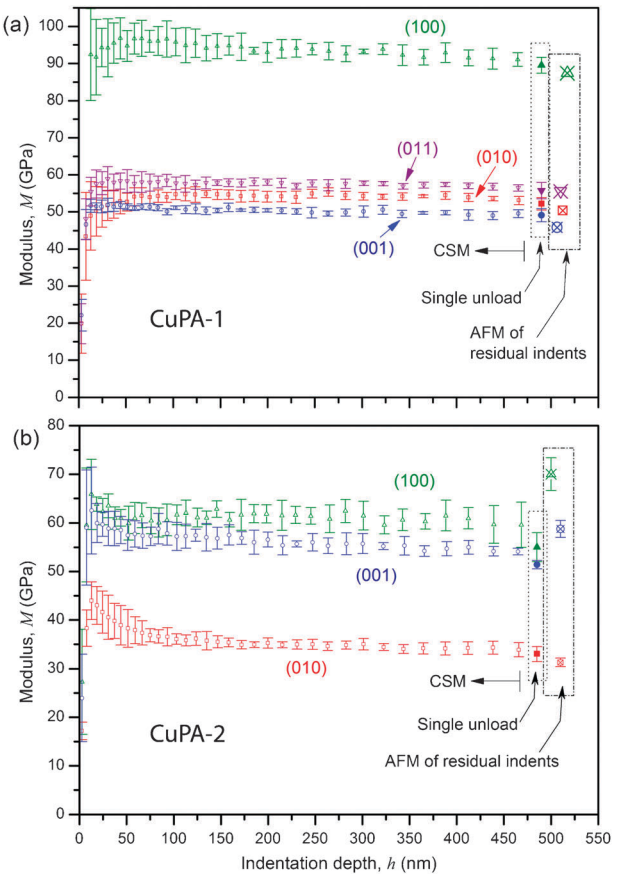

Fig. 4 Elastic moduli determined along the main crystallographic orientations of (a) CuPA-1 and (b) CuPA-2. The data were obtained from three different methods using a Berkovich nanoindenter. "CSM" denotes Continuous Stiffness Measurement,[52] which has the advantage of collecting depth-dependent mechanical data, while the "single unload" experiment is the conventional method that derives the stiffness property from the initial part of the unloading slope. The third method accounts for pile-up corrected moduli based on the AFM profiles of residual indents. Adapted from ref. 30.

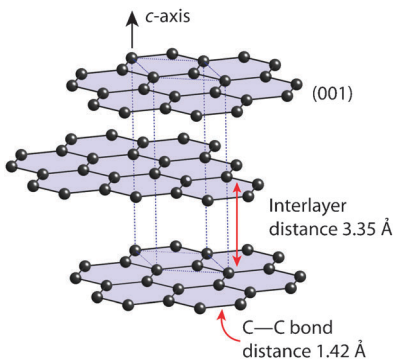

Fig. 5 Graphite has a very anisotropic crystal structure with strong covalent bonds lying in the {001}-oriented planes but weak interatomic interactions between the adjacent layers.

3.35 Å) resulted in small elastic stiffness down the transverse direction (*c*-axis). Quite remarkably, the C_{11} and C_{22} elastic constants (signify in-plane stiffnesses) in graphite are similar to those of diamond and of single-layered graphene sheet, *i.e.* ≈1060 GPa; but its C_{33} value (denotes out-of-plane stiffness) is appreciably lower at only 36.5 GPa.[56] Indeed, we notice that the latter is of a similar magnitude to that of CuPA-2 normal to the H-bonded layers, *i.e.* $E_{(010)} \approx 35$ GPa (Fig. 4(b)),[30] which could be attributed to their similar inter-layer bond energies.

(b) Lanthanide mixed-ligand framework. Tan *et al.*[31] reported a subsequent nanoindentation study on single crystals of cerium oxalate formate, $Ce(C_2O_4)(HCO_2)$,[57] to investigate how the elastic anisotropy of dense hybrid frameworks are controlled by the underlying architectures. This mixed-ligand hybrid compound (Fig. 6) crystallizes with an orthorhombic crystal structure and hence presents the unique architecture appropriate for decoupling the mechanical responses along its three primary axes. Information obtained was used to access the contribution associated with stiff *versus* compliant basic building blocks. Herein, the three building blocks are the inorganic M–O–M chains and the two organic bridging ligands, *i.e.* the oxalate ($C_2O_4^{2-}$) and the formate ($HCOO^-$) ions; these are effectively oriented perpendicular to one another (Fig. 6(b)). Between the two ligands, it is well established that the former is structurally more rigid than the latter.[13]

Nanoindentation results (Fig. 7) unambiguously show that the (001)-oriented facet that features rigid oxalate ligands down the *c*-axis exhibits the highest Young's modulus ($E_{(001)} \approx 78$ GPa). Conversely, the (010)-oriented facet appears to be the most compliant ($E_{(010)} \approx 43$ GPa) since the formate ligand, which is the more flexible building block, constitutes the primary linkages down the *b*-axis. The intermediate stiffness measured on the (100)-oriented plane (≈52 GPa) can be attributed to not only the Ce–O–Ce inorganic chains that zig-zag down the *a*-axis (Ce···Ce metal centers form an angle

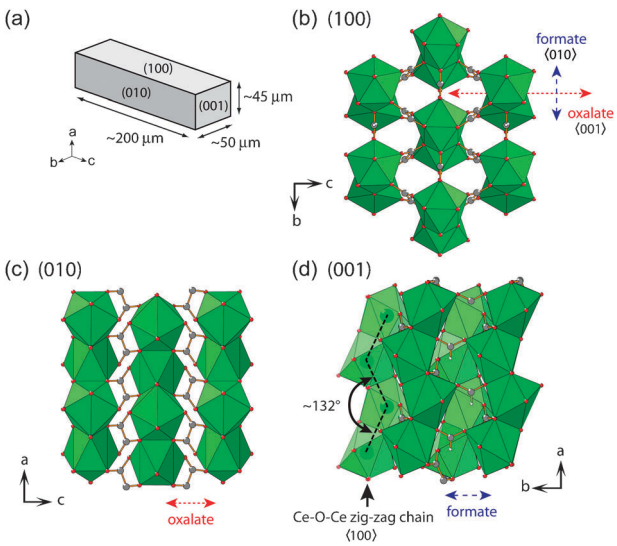

Fig. 6 The crystal structure of $Ce(C_2O_4)(HCO_2)$ dense hybrid framework. (a) The typical single crystal morphology (habit) and its low index faces. (b)–(d) Views perpendicular to the (100), (010) and (001) planes respectively, *i.e.* normal to the orientation of the nanoindenter axis. Green: cerium; gray: carbon; red: oxygen; white: hydrogen. Adapted from ref. 31.

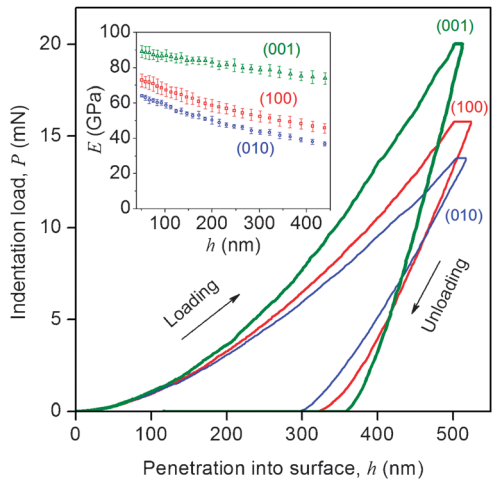

Fig. 7 Nanoindentation results on cerium oxalate formate single crystals given in Fig. 6. The representative load-displacement (*P–h*) curves were obtained using a sharp Berkovich tip along its three main crystallographic orientations. The inset presents the elastic moduli data as a function of indenter penetration depth, the gradual decrease in CSM stiffness data may be associated with subsurface cracking. Adapted from ref. 31.

of 132°, see Fig. 6(d)), but also to their high-coordination polyhedra (CeO_9) that are geometrically more compliant.

This study amounts to the fact that crystallographic orientation dominated by the M–O–M inorganic chains (*i.e.* coordination-bonded building blocks) is not necessarily more robust from the mechanical properties standpoint. Instead, a greater elastic stiffness could be effected by means of rigid organic bridging linkers (such as covalently-bonded oxalates) strategically oriented along a predefined crystal axis. This example illustrates a general principle whereby the combination of organic multifunctional ligands of different rigidities and bond energies can potentially be exploited through crystal engineering[49,50] to "design" and tailor the required mechanical properties.

(c) Probing elastic anisotropy by density-functional calculations. Kosa *et al.*[32] recently demonstrated the application of computational and experimental approaches to elucidate the elastic anisotropy of zinc phosphate phosphonoacetate (ZnPA): $Zn_3(PO_4)(O_2CCH_2PO_3)(H_2O)$ (Fig. 8). This 3-D framework is composed of Zn–O–Zn layers that are connected by phosphate groups bridging the ZnO_4 tetrahedra, which in turn section off small channels that run parallel to the *a*-axis. Although the small voids constitute non-accessible porosity (Fig. 8(b)), computational results indicate that the pore morphology can nevertheless contribute towards elastic anisotropy. An efficient computational scheme based on Density-Functional Theory (DFT) (within the general gradient approximation (GGA)) has been proposed for estimating the Young's modulus and the Poisson's ratio (ν) along the principal crystal axes. Notably, this approach can circumvent the intricacies in computing the full elastic stiffness tensor (C_{ij}), which often proves to be cumbersome for low-symmetrical crystal systems (*e.g.* ref. 58 and 59).

The relative stiffnesses of the different crystal facets, calculated using the proposed scheme, were found to be

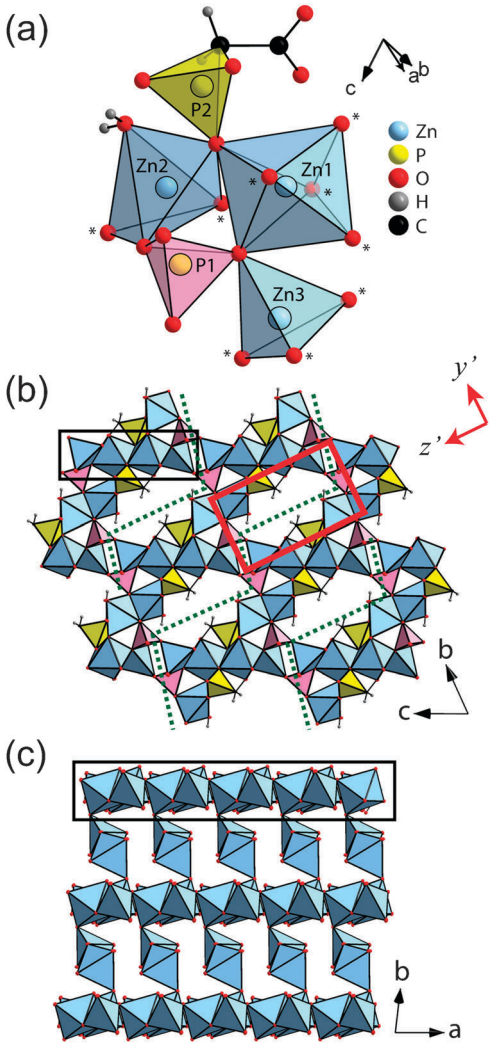

Fig. 8 The crystal structure of $Zn_3(H_2O)(PO_4)(O_2CCH_2PO_3)$, ZnPA. (a) The asymmetric unit, wherein the zinc polyhedra are in blue, PO_4 tetrahedron is in pink and PCO_3 tetrahedron in yellow. (b) View of the channels along the *a*-axis and the red outline encloses an elliptical cavity. The adjacent Zn–O–Zn layers are highlighted by the green dotted lines while a ZnO_x ribbon is outlined in black. (c) View of the ZnO_x layered structure down the *c*-axis, PO_4 and PCO_3 tetrahedra are here omitted for clarity. Adapted from ref. 32.

in reasonably good agreement with experiments (Table 1). Of which, the theoretical and experimental anisotropy ratios pertaining to the Young's moduli are $E_x : E_y : E_z = 1.34 : 1.00 : 1.11$ and $E_{(100)} : E_{(010)} : E_{(001)} = 1.25 : 1.00 : 1.16$, respectively. In terms of their absolute values, however, the calculated moduli are consistently higher, by as much as 25% to 40%, than those determined experimentally. Given that the hybrid compound considered here is not moisture sensitive (effects of crystal degradation is negligible), the Young's moduli measured by nanoindentation according to the procedures previously established in ref. 30 and 31 are expected to be reliable.

This study[32] pointed out that the higher stiffnesses calculated by DFT could be ascribed to factors arising both from the derivation scheme as well as deficiencies associated with the electronic structure methods used. With regard to the

Table 1 Measured and calculated anisotropic elastic properties of ZnPA. Adapted from ref. 32

	Single-crystal nanoindentation		DFT calculation	
Young's modulus, E (GPa)	$E_{(100)}$	53.34 ± 1.50	E_x	74.56
	$E_{(010)}$	42.57 ± 0.93	E_y	55.44
	$E_{(001)}$	49.59 ± 1.32	E_z	61.51
Poisson's ratio, ν_{ij}	Not measured[a]		$\nu_{xy} = 0.26$	$\nu_{yx} = 0.19$
			$\nu_{xz} = 0.35$	$\nu_{zx} = 0.29$
			$\nu_{yz} = 0.37$	$\nu_{zy} = 0.29$

[a] The sample Poisson's ratio was taken as 0.2. In fact, the calculated value of E from the Oliver and Pharr method[52] is not particularly sensitive to the absolute value of ν. For instance, a 50% increase in ν from 0.2 to 0.3 gives only a 5% difference in the corresponding values of E.

derivation scheme, for instance, theoretical calculations at 0 K are expected to overestimate the elastic stiffnesses as opposed to experiments performed at ambient conditions ($\approx$300 K). In relation to the electronic structure method, it is noted that incorrect description of the position of transition metal *d*-states can cause over-hybridization of the Zn–O bonds within GGA because of self-interaction error (SIE);[60] this amounts to "artificial stiffening" in the zinc–oxygen cores of the ZnPA framework. More generally, due to the current limitations pertinent to DFT,[61,62] one should realize that elastic property predictions for complex hybrid systems are potentially sensitive to the choice of, among others, the exchange–correlation functional and the pseudopotential.

2.1.2 Nanoporous hybrid frameworks

(a) MOF-5. Bahr *et al.*[36] were among the first who attempted to characterize the elastic properties of a MOF-type material by employing both experimental and computational means. They chose the well-known ZnO_4-based open framework structure designated as MOF-5 (or IRMOF-1): $ZnO_4(BDC)_3$; BDC = 1,4-benzenedicarboxylate.[63] Through single-crystal nanoindentation, the average elastic modulus was measured as $E = 2.7 \pm 1.0$ GPa. But after accounting for the contribution of elastic anisotropy in a cubic crystal,[53] they estimated the Young's modulus of the (100)-oriented facet to be 7.9 GPa. On the other hand, their DFT calculations (average of local density approximation (LDA) and GGA) resulted in Young's moduli of $E_{(100)} = 21.6$ GPa and $E_{(111)} = 7.5$ GPa, signifying an anisotropy factor of $E_{\{100\}}/E_{\{111\}} = 2.88$. This indicates that the stiffer direction corresponds to the $\langle 100 \rangle$ principal axes (Fig. 9), which are indeed parallel to the rigid organic BDC linear linkers.

Notably, we observe that the calculated value of $E_{(100)}$ is about a factor of three times greater than its experimental value. Other independent DFT studies have produced similar outcomes (Table 2), with the values of $E_{(100)} \approx 22$ GPa and $\nu = 0.28$–0.31 at 0 K. Molecular dynamics (MD) studies employing force fields have generally predicted even higher stiffnesses. For instance, the results of Han and Goddard[39] shown that $E_{(100)} \approx 42$ GPa at 10 K (*NB*: about twice that of DFT at 0 K) and this decreases to $\approx$31 GPa at 300 K (Fig. 10(b)). Greathouse and Allendorf[37] also reported a higher Young's modulus of 35.5 GPa at 0 K; but at 300 K, they predicted an appreciably lower value of 14.9 GPa. Computational results so far suggest that even if we factor in the effects of thermal fluctuations, the calculated values still remain noticeably higher than experimental observations.

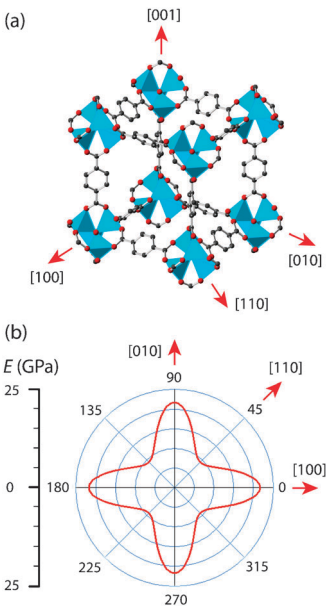

Fig. 9 Anisotropic elastic stiffness of a cubic MOF-5 single crystal. (a) Crystal structure and its principal axes. Blue: zinc; gray: carbon; red: oxygen. (b) Young's modulus (E) as a function of crystallographic orientations, here plotted in the *a*–*b* plane under rotation about the *c*-axis. E was determined based on the three independent elastic constants calculated by DFT:[36] $C_{11} = 28.2$ GPa, $C_{12} = 11.4$ GPa and $C_{44} = 2.7$ GPa (LDA-GGA averaged values, see Table 2).

From the experimental perspective, such discrepancies can be partly ascribed to physical degradation of the crystals. It has been established that MOF-5 exhibits poor hydrothermal stability and decomposes rapidly in humid conditions, especially upon removal from the mother liquor.[64,65] Furthermore, detailed mechanisms surrounding water-induced disruption in MOF-5 has recently been elucidated *via* MD simulations, from which the structure is projected to collapse at just 4.5 wt% H_2O.[66] An important consequence is that nanoindentation measurements performed on (partially) decomposed compound are expected to yield a much lower stiffness property compared to that of a pristine crystalline structure.

On the basis of the computed Young's modulus of MOF-5 alone, as summarized in Table 2, it is therefore not possible to comment on the accuracy of existing theoretical approaches for determining the elasticity of nanoporous hybrid frameworks. Yet from the computational standpoint, we emphasize that by having zinc-oxygen cores, the electronic structure of MOF-5 is indeed reminiscent to that of bulk ZnO.

Table 2 Summary of the elastic properties MOF-5 (IRMOF-1) calculated by computational methods. The elastic constants C_{ij} is shown as a function of temperature (when data are available). The bulk modulus is given by $K = (C_{11} + 2C_{12})/3$. The Young's modulus on the {100}-oriented facets of a cubic cell is determined by $E_{(100)} = [(C_{11} + 2C_{12})(C_{11} - C_{12})]/(C_{11} + C_{12})$. The Poisson's ratio is found by $\nu = C_{12}/(C_{11} + C_{12})$. Experimental result at ambient conditions: Bahr *et al.*[36] reported $E_{(100)} = 7.9$ GPa from nanoindentation of single crystals

Source	*Year Published*	*Method*	*Computational Details*	*Temp. (K)*	C_{11} (GPa)	C_{12} (GPa)	C_{44} (GPa)	K (GPa)	$E_{(100)}$ (GPa)	ν
Zhou and Yildrim[33]	2006	DFT	LDA, USP	0	29.42	12.56	1.16	18.18	21.90	0.30
Samanta *et al.*[34]	2006		LDA, PAW		29.2	13.1	1.4	18.5	21.1	0.31
Mattesini *et al.*[35]	2006		LDA, Norm conserving		21.52	14.77	7.54	17.02	9.50	0.41
Bahr *et al.*[36]	2007		LDA, PAW		27.8	10.6	3.6	16.3	21.9	0.28
			GGA, PAW		28.5	12.1	1.7	17.6	21.3	0.30
			Average LDA–GGA		28.2 ± 0.4	11.4 ± 0.8	2.7 ± 1.0	17.0 ± 0.6	21.6	0.29
Han and Goddard[39]	2007	MD	DREIDING force field	10	44.53	6.79	1.82	19.37	42.73	0.13
				300	34.13	7.93	1.36	16.66	31.14	0.19
Greathouse and Allendorf[37]	2008		CVFF force field	0	—	—	—	20	35.5	—
				300	—	—	—	4	14.9	—
Tafipolsky and Schmid[38]	2009		MM3(2000) force field	0	25.3	8.9	2.3	14.4	20.67	0.26
				300	≈ 21.5	≈ 5.3		≈ 10.8		

Numerous computational studies reported on the elastic properties of ZnO (*e.g.* ref. 67–69) have already revealed a large spread and inconsistencies in the predicted C_{ij} data. In consequence, one needs to be aware of the deficiencies associated with the LDA and GGA approximations when applying DFT to model strongly-correlated systems widely encountered in hybrid frameworks (*e.g.* ref. 32). We also observe that while MD simulations offer the additional benefit of being able to capture the effects of temperature variation, their results appear to be somewhat sensitive towards the choice of force fields (Table 2).

(b) Temperature-dependent elasticity of IRMOFs. Isoreticular metal–organic frameworks (IRMOFs) represent one of the most studied MOF classes in regard to their unique structures and functional characteristics.[70] In this section, we examine their temperature-dependent elastic properties, in particular E and ν, by considering a range of isoreticular frameworks depicted in Fig. 10(a). Each structure contains the $Zn_4O(CO_2)_6$ connector that is coupled to six aromatic linkers through the O–C–O moiety common to each linker. Here, we can only discuss finite-temperature MD predictions[39] because the corresponding experiments are not yet available. Nonetheless, our current focus is more towards understanding the general trends and less about the absolute values.

The effects of temperature on elastic properties are generally important and become significant for systems with weaker chemical bonding and/or flexible organic ligands. As temperature rises, most materials turn more compliant as the amplitude of thermal vibrations increases, resulting in longer interatomic distances and therefore weaker chemical bonds. From Fig. 10(b)–(c), it is evident that the Young's moduli of all isoreticular structures are strongly dependent not only on the framework density and pore volume, but also on the temperature. First, we observe that the elastic stiffness property of IRMOFs increases rapidly as the framework turns denser; interestingly, such a characteristic is also reminiscent of macroporous cellular solids (*e.g.* metallic foams).[71] Second, there exists a strong inverse correlation with respect to the degree of openness of the hybrid framework, as represented by the pore accessible volume presented in Fig. 10(c). Depending on the structure, we observe that as the temperature rises from 10 K to 300 K, the predicted elastic moduli decrease by about 20%–30%.

At 10 K, the Poisson's ratios (ν) of IRMOFs considered here fall within the narrow range of 0.13–0.16,[39] which are much lower than DFT predictions at a similar temperature (MOF-5: $\nu = 0.28$–0.31 at 0 K).[33,34,36] In any event, the general trend is that the Poisson's ratio decreases as the temperature rises for all IRMOFs incorporating aromatic linkers bulkier than the BDC. On the contrary, the MD simulations[39] clearly indicate that the Poisson's ratio of MOF-5 increases by about 50% upon heating to 300 K (*i.e.* ν rises from 0.13 to 0.19). The reason behind such a phenomenon is not yet clear, and could be attributed to its relatively small shear modulus (see section 2.3.1).

(c) Zeolitic imidazolate frameworks (ZIFs). ZIFs represent a unique class of MOF material that combines the outstanding chemical and thermal stability of inorganic zeolites with the rich topological diversity characteristic of MOFs.[72] The structure of ZIFs (Fig. 11) consists of tetrahedral metal centers (typically M = Zn^{2+} or Co^{2+}) that are solely coordinated by nitrogen atoms in the 1,3-positions of the imidazolate bridging ligand (Im = $C_3N_2H_3^-$), subtending an angle of 145° at the M–Im–M center.[73,74] This is indeed analogous to the Si–O–Si angle in silicas and zeolites, therefore ZIFs can adopt zeotype topologies to afford a multitude of 3-D open framework structures. Over 100 distinct ZIF phases based on 36 tetrahedral topologies (nets) have been identified to date, and these include new topologies yet to be discovered in inorganic zeolites.[75,76] A huge amount of activity now exist in this area, especially on the design and optimization of their functional properties for a wide range of practical applications.[17,77,78]

The Young's modulus of ZIFs, however, have remained unexplored until recently when Tan *et al.*[44] employed single-crystal nanoindentation to establish their structure–mechanical property behavior in relation to the chemical structure, network topology and porosity. To broadly represent the cross-section of ZIFs reported thus far, 7 ZIF phases (ZIF-zni, -4, -7, -8, -9, -20 and -68, see Fig. 12) based on 5 unique network topologies (zni, cag, SOD, LTA and GME) have been considered. Nanoindentation data clearly indicate

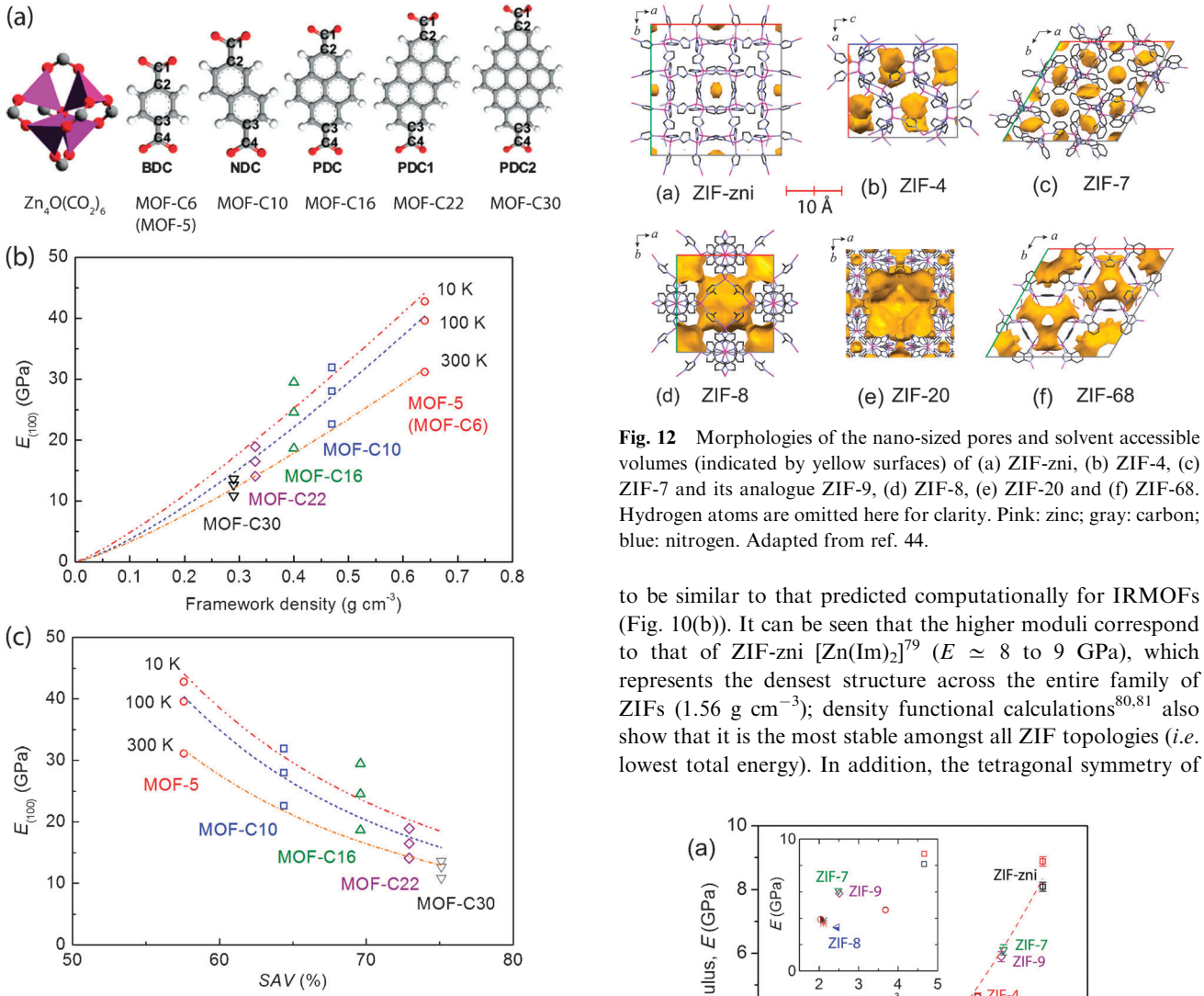

Fig. 10 (a) IRMOFs considered for finite-temperature MD simulations, each structure is named according to the number of aromatic carbon atoms. Here note that MOF-C6 is indeed equivalent to MOF-5. The Young's modulus along the (100)-oriented facet as a function of (a) the framework density and (b) the porosity (%SAV) were calculated from the C_{11}, C_{12} and C_{44} elastic constants reported in ref. 39. The curves serve as guides to showcase the general trend corresponding to temperatures of 10, 100 and 300 K. Panel (a) is adapted from ref. 39 with permission, copyright (2007) American Chemical Society.

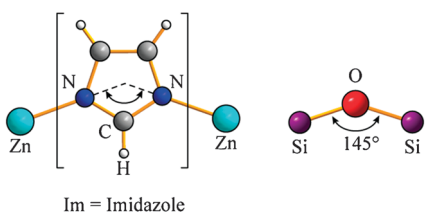

Fig. 11 Representations of the Zn–Im–Zn and Si–O–Si linkages in tetrahedral ZIF and silicate networks, respectively. Adapted from ref. 45.

that the elastic moduli of the different ZIF systems scale non-linearly with respect to the framework density (Fig. 13), whereby the framework elastic stiffness increases considerably as the structure turns denser. Notably, such a response appears

Fig. 12 Morphologies of the nano-sized pores and solvent accessible volumes (indicated by yellow surfaces) of (a) ZIF-zni, (b) ZIF-4, (c) ZIF-7 and its analogue ZIF-9, (d) ZIF-8, (e) ZIF-20 and (f) ZIF-68. Hydrogen atoms are omitted here for clarity. Pink: zinc; gray: carbon; blue: nitrogen. Adapted from ref. 44.

to be similar to that predicted computationally for IRMOFs (Fig. 10(b)). It can be seen that the higher moduli correspond to that of ZIF-zni [$Zn(Im)_2$][79] ($E \simeq 8$ to 9 GPa), which represents the densest structure across the entire family of ZIFs (1.56 g cm^{-3}); density functional calculations[80,81] also show that it is the most stable amongst all ZIF topologies (*i.e.* lowest total energy). In addition, the tetragonal symmetry of

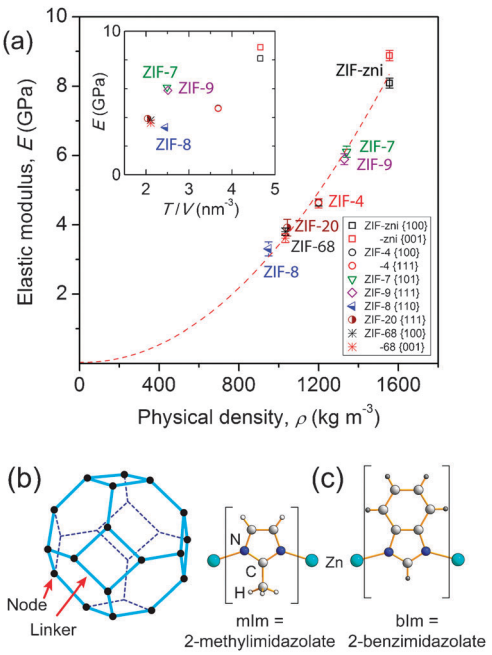

Fig. 13 Elastic modulus of ZIF single crystals. (a) E as a function of the framework physical density and number of tetrahedral (metal) sites per unit volume (*i.e.* T/V in inset). The modulus–density correlation can be approximated by a quadratic relationship represented by the red dotted curve. (b) The sodalite (SOD) cage for ZIF-7, -8 and -9, wherein the node is Zn(II) or Co(II) while the linkers are substituted imidazolates. (c) Representations of the Zn–mIm–Zn and Zn–bIm–Zn linkages found in ZIF-8 and ZIF-(7, 9) respectively. Adapted from ref. 44.

ZIF-zni also gives rise to elastic anisotropy indicated by the differential moduli in the {001}- and {100}-oriented facets, whereby the anisotropy factor $E_{\{001\}}/E_{\{100\}} \simeq 1.1$. It is noteworthy that due to its relatively high density, the elasticity of ZIF-zni somewhat resembles those reported in fully dense hybrid systems, whose stiffnesses are of the order of 10 GPa (Fig. 2).[30–32] On the other hand, ZIF-8, -20 and -68 that are representative of low-density open frameworks ($\rho < 1.0$ g cm^{-3}) are indeed compliant structures exhibiting comparatively low stiffnesses ($E \approx 3$–4 GPa).

Fig. 14(a) shows that the Young's moduli of ZIFs exhibit strong inverse correlation with respect to the internal accessible void space (defined as solvent accessible volume, *SAV*). Again, all highly porous frameworks with *SAV* approaching values of 50% (*e.g.* ZIF-8, -20 and -68) display consistently lower elastic stiffnesses. Such a correlation also suggests that open frameworks of even higher porosities than those studied here, for example the ZIF-95 and -100 phases featuring poz and moz topologies respectively,[82] could be very compliant structures with moduli likely to be of only a few GPa or less.

The work of Tan *et al.*[44] further demonstrates that when considering ZIFs of the same topology, the structures incorporating sterically bulky (substituted) imidazolate ligands confer greater stiffnesses as a result of short-range ligand-ligand interactions. This can commonly be associated with large aromatic linkers that tend to project into the pore regions, thereby inducing a higher degree of pore space filling. To illustrate, the elastic properties of three sodalite (SOD) ZIFs were considered: ZIF-7, -8 and -9, which possess the same network topology but incorporating two markedly different functionalized groups (Fig. 13(b–c)). Notably, the Young's moduli of the analogous ZIF-7 and -9 structures

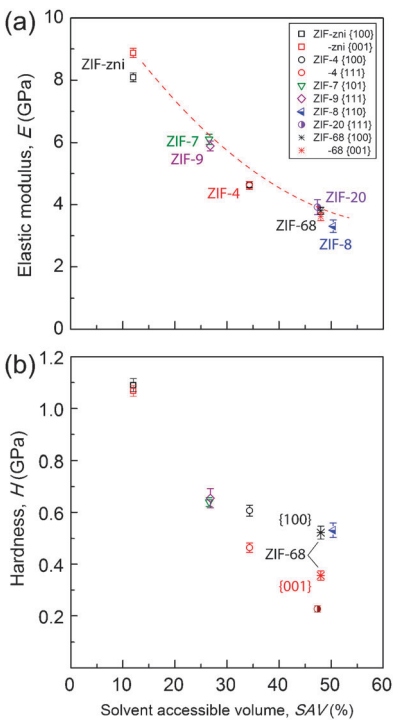

Fig. 14 (a) Elastic modulus and (b) nanohardness of ZIFs as a function of pore accessible volume. Adapted from ref. 44.

(Zn^{2+} and Co^{2+} tetrahedral centers respectively) were found to be a factor of two greater than that of ZIF-8 (Fig. 13(a) inset). Indeed, the 2-benzimidazolate (bIm) linkages in ZIF-7 and -9 are sterically bulkier compared to the 2-methylimidazolate (mIm) in ZIF-8. The integration of sterically bulky organics as part of the open framework structure can induce additional short-range dispersive interactions (van der Waals) contributing to a greater stiffening of the hybrid structure. Perhaps not surprisingly, it was also demonstrated that for ZIFs containing similar transitional metal centers (*e.g.* ZIF-7 and -9), their elasticity are largely controlled by the relatively rigid imidazolate building blocks; whereas the metal-centered tetrahedral sites (ZnN_4 or CoN_4 in ZIF-7 and -9 respectively) serve only as "flexible" coordination environments (*i.e.* compliant nodes) for connecting adjacent linkages. Such a characteristic is consistent with the findings of recent experimental[83,84] and theoretical[39] studies concerning rigid organic linkers.

(d) Boron imidazolate frameworks (BIFs). A deeper insight into the contribution of the MN_4 coordination environment flexibility and bond stiffness toward elasticity can be gained by comparing the mechanical properties of the "dense" ZIF-zni (*i.e.* $Zn(Im)_2$, 12% *SAV*) with its lightweight $LiB(Im)_4$ analogue (Fig. 15).[46] The latter is also designated as BIF-1-Li,[85] and it belongs to Boron Imidazolate Frameworks (BIFs) which are the I–III analogues of the ZIFs, with alternate Zn cations being replaced by Li and B respectively.[85,86] Notably, both ZIF-zni and $LiB(Im)_4$ adopt the same zni topology as the banalsite mineral.[87]

It is startling to observe that the Young's moduli of ZIF-zni as measured by nanoindentation (Fig. 15(e)) are three times greater than those of $LiB(Im)_4$ ($E = 2.7$ to 3.3 GPa).[46] Given that both frameworks are isostructural, the large difference in terms of their moduli indicates that the Zn–Im–Zn bonds of ZIF-zni are considerably stiffer than the predominantly ionic bonds associated with the Li–Im–B linkages of the lightweight counterpart. Through high-pressure X-ray diffraction experiments and DFT calculations (section 2.2.2), it was further established that the structure of $LiB(Im)_4$ consists of metal coordination polyhedra of both higher (BN_4) and lower (LiN_4) bond energies. Because LiN_4 represents the flexible and compliant motif, it is hypothesized that the weaker lithium environment dominates the Li–Im–B linkage deformation when subjected to an indentation loading, thus conferring low elastic stiffness properties.[46]

(e) Host–guest interactions on elasticity. Effects of pore occupancy on the elasticity of a prototypical ZIF-8 single crystal have been reported.[44] In particular, the high hydrothermal stability of ZIF-8[65] in combination with its relatively large solvent accessible volume (50.4% *SAV*) make it an ideal candidate for such a study. Nanoindentation experiments conducted on the {110}-oriented facets of ZIF-8, confirmed the permanent porosity characteristic of ZIFs, and further established the reversible nature relating to guest uptake–removal exhibited by robust MOF-type materials (*e.g.* ref. 88 and 89). In ZIF-8, the desolvated crystal was found to exhibit marginally lower elastic properties

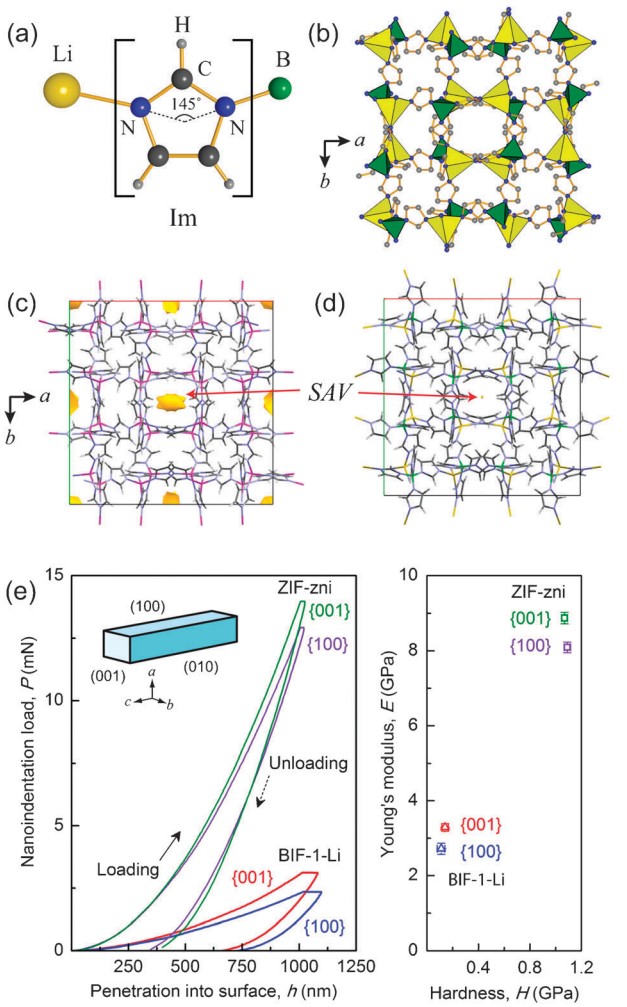

Fig. 15 (a) The basic inorganic–organic connectivity of $LiB(Im)_4$ [BIF-1-Li], note the subtended angle of 145° at the imidazolate (Im) bridging ligand. (b) The unit cell of $LiB(Im)_4$ viewed down the [001]-direction. The yellow and green tetrahedra designate LiN_4 and BN_4 respectively, hydrogen atoms are omitted here for clarity. (c) The *SAV* of ZIF-zni [$Zn(Im)_2$] down the *c*-axis, in comparison to the much smaller accessible volume present in (d) $LiB(Im)_4$ viewed along the same orientation. Pink: zinc; gray: carbon; blue: nitrogen; green: boron; yellow: lithium. (e) Nanoindentation results of the two zni analogues. Left panel: representative nanoindentation curves along the {100} and {001} facets (Inset: typical crystal habit). Right panel: the average values of Young's moduli and hardness properties. Adapted from ref. 46.

(*E* decreases by ≈7%), but the original stiffness can be recovered upon subsequent exposure to DMF molecules (*N*,*N*-dimethylformamide). This is a fine demonstration of the guest-dependent dynamic behavior of MOFs with regard to elasticity,[22] central to the operation of stress-induced chemical sensing devices like the ones communicated by Allendorf *et al.*[26]

Other MOF-type materials with highly flexible frameworks, can experience very large volume increases (*i.e.* swelling) upon solvent adsorption. For example, the MIL-88 (MIL = Materials from Institut Lavoisier) structures are capable of "breathing motion" by undergoing a reversible coordinated atomic movement of greater than 10 Å, all without the loss of crystallinity.[90] Given that MILs are synthesized in the form of powders, the impact of host–guest interactions on the framework elastic properties cannot be directly measured *via* nanoindentation (as demonstrated in ZIF-8 single crystals[44]). Instead, Demessence *et al.*[47] developed a dip-coating approach to prepare thin films from nanoparticles of MIL-101(Cr), a chromium terephthalate-based MOF with a cubic zeotype architecture. Upon water adsorption, the transverse Young's modulus of the nanoparticles (22 ± 5 nm) was measured using spectroscopic ellipsometry and the average stiffness value was found to be 17 ± 10 GPa (calculated from contraction isotherm[91]). Even if we consider the somewhat large uncertainty associated with the moduli data (±60%), the stiffness of the nanoparticles after guest uptake is still appreciably high, and is of the order of dense ZIF-zni phase (8–9 GPa). However, they did not report the stiffness of the nanoparticles in the evacuated state. Rather surprisingly, the Young's modulus of the MIL-101(Cr) thin film fabricated from such nanoparticles was found to be of three orders of magnitude smaller under the adsorbed state, *i.e.* $E = 40 \pm 10$ MPa.[47] The exceedingly compliant nature of the deposited film is most likely attributed to nanoparticles that are weakly bonded together (through van der Waals and electrostatic forces).[92] In addition intergrain mesopores and microcracks present at the microstructural level can further reduce the effective stiffness of the deposited film.

2.2. Bulk modulus and compressibility

The bulk modulus, *K* (*i.e.* the inverse of compressibility) is a measure of volumetric elasticity and signifies the mechanical resistance of a material against volumetric changes (strains) under uniform hydrostatic pressure. In relation to hybrid framework materials, a number of experimental and theoretical studies have been reported to determine their compressibility over a range of pressures, to investigate pressure-induced phase transformation phenomena, and to understand the effects of hydrostatic loading on the flexibility of basic building blocks.

2.2.1 High-pressure crystallography of ZIFs. Reported experimental studies involve subjecting MOFs in the form of single crystals[43,46,84] or powders[25,40] to hydrostatic compression in a diamond anvil cell (DAC) filled with a pressure-transmitting medium. Pressurization was carried out typically up to a level of several GPa. Based on the pressure-induced changes in lattice volume obtained from high-pressure X-ray diffraction, the bulk moduli (*K*) of MOFs were determined from the Birch-Murnaghan equation of state.[93]

Using such an approach, Spencer *et al.*[43] estimated the room-temperature bulk modulus of the densest ZIF phase, *i.e.* $Zn(Im)_2$ (or ZIF-zni) to be ≈14 GPa. Furthermore, at higher pressures of between 0.54 and 0.85 GPa, it underwent a phase transition while maintaining the original tetragonal crystal system (space group transforms from $I4_1cd$ to $I4_1$). This transformation can be attributed to a complex cooperative bond rearrangement mechanism. Likewise, Chapman *et al.*[25] estimated the bulk modulus of nanoporous ZIF-8 but found it to be much lower at $K \approx 6.5$ GPa. Given the compliant nature of ZIF-8 (Section 2.1.2(c)), the framework compresses rapidly

and undergoes a large volumetric change of about 5% over 0.3 GPa. Pressurization beyond 0.34 GPa leads to an irreversible structural transition and amorphization upon recovery to ambient pressure. Here we emphasize that amorphized ZIFs, or indeed ones with distorted or collapsed structures, are unlikely to retain the exceptional sorption, separation and catalytic properties associated with pristine crystalline materials. Clearly, structurally robust MOFs are highly desirable for industrial applications whereby external pressures of several GPa are commonplace.

Indeed, a materials property map of bulk moduli *vs.* physical density can be constructed as in Fig. 16 to clearly demonstrate the compressibility of nanoporous hybrid frameworks in comparison with other classes of (porous) materials. Again, it is striking to observe that the domain that corresponds to MOFs somewhat straddles the borders between the organic polymers, foams (including metallic, ceramic and polymeric foams with macroscale porosity (pore size ranging from hundreds of μm to several cm)), inorganic ceramics and also nanoporous aluminosilicate zeolites. Given their inorganic network architectures and higher framework densities, the K values of inorganic zeolites by and large fall in the range of 20–70 GPa, which are generally higher than MOFs. For instance, the bulk modulus of a zeolite with the SOD topology is about five times greater than that of its ZIF counterpart (ZIF-8).

2.2.2 Pore volume *versus* tetrahedral flexibility. The hydrostatic compression behavior of the lightweight $LiB(Im)_4$ framework has recently been studied by Bennett

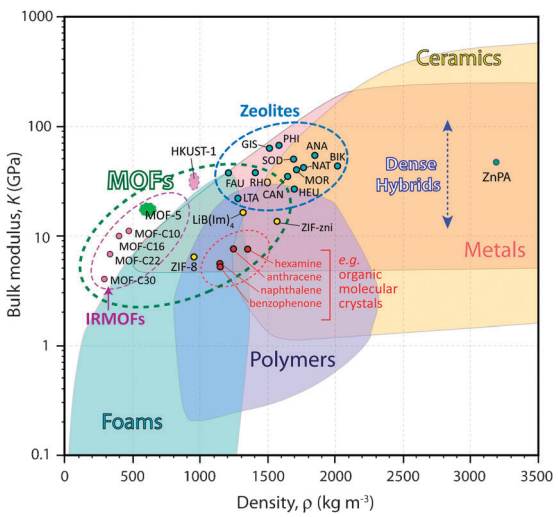

Fig. 16 Bulk modulus *versus* physical density material property map for hybrid frameworks, plotted alongside other major classes of materials. Data sources for hybrids: ZnPA,[32] MOF-5 (DFT results at 0 K),[33–36] HKUST-1 (high-pressure crystallography[40] and MD results),[41,42] MOF-C10, -C16, -C22 and -C30 (MD results at 300 K),[39] ZIF-zni,[44] $LiB(Im)_4$.[46] Examples of organic molecular crystals were obtained from ref. 95. Bulk moduli data (prior to phase transition) of a wide range of inorganic zeolites of different topologies: Natrolite (NAT),[127] Analcime (ANA),[128] Phillipsite (PHI),[129] Gismondine (GIS),[130] Sodalite (SOD),[131] Zeolite-A (LTA),[132] Zeolite-Y (FAU),[133] Cd-RHO (RHO),[134] Mordenite (MOR),[128] Bikitaite (BIK),[135] Heulandite (HEU),[136] and Cancrinite (CAN).[137]

et al.,[46] from which interesting observations can be drawn through comparison with its isostructural, heavier zinc-containing analogue ZIF-zni [$Zn(Im)_2$]. Despite its much lower density (ρ = 1.31 g cm^{-3}), the bulk modulus of $LiB(Im)_4$ was found to be 16.6 GPa, indicating that the framework is indeed less compressible than ZIF-zni ($K \approx$ 14 GPa,[43] ρ = 1.56 g cm^{-3}). The former also undergoes a phase transition at 1.69 GPa, which is twice of that reported for its heavier counterpart.

Notably, no significant change in the Li–N, B–N, and Zn–N bond lengths upon pressurization was observed. However, a direct comparison of the spread of N–M–N angles (M = metal) at each pressure level revealed the sequence of flexibility of the metal coordination environment to be LiN_4 > ZnN_4 > BN_4. Therefore, it is intriguing that $LiB(Im)_4$ exhibits a lesser compressibility and a higher phase transition pressure, despite evidence to the contrary in view of the more flexible and deformable nature of the lithium coordination environment. Such a phenomenon may be rationalized by the lighter framework having a smaller pore volume, hence rendering it less able to accommodate volumetric strains. Fig. 15(c–d) shows that, while being isostructural, the cell volume of ZIF-zni is indeed around 23% larger than that of $LiB(Im)_4$ with the SAV within each framework being 12.2% and 5.3%, respectively.

2.2.3 Guest-dependent high-pressure phenomena. Another high-pressure study reported by Chapman *et al.*[40] shows that the compressibility of the nanoporous Cu-BTC framework (or HKUST-1, $Cu_3(BTC)_2$; BTC = 1,3,5-benzenetricarboxylate)[94] is strongly dependent upon the type of pressure-transmitting media. Specifically, by subjecting the open framework to pressure-transmitting fluid molecules of different sizes and to high pressures (maximum of 8 GPa), they observed a dramatic transition between a "hard" regime ($K \approx$ 118 GPa) and a "soft" regime ($K \approx$ 30 GPa) (Fig. 17). The regime of greater bulk moduli occurs at lower pressures and is associated with pressure-induced hyperfilling (*i.e.* progressive filling of accessible pore volume by smaller guest molecules), so that the system appears to be of a much lower compressibility. Beyond the threshold pressure, however, the guest-framework system compresses concertedly due to a reduced rate of guest inclusion at higher pressures, subsequently giving rise to lower bulk moduli.

Such an unprecedented pressure-induced phenomenon in MOFs depends not only on the size of the pressure-transmitting fluid molecules, but also on the pressurization (strain) rate and the particulate size of polycrystalline powders. Indeed, a similar pressure-induced behavior was reported for ZIF-8 in which a phase transition was detected at 1.47 GPa.[84] Detailed examination of the crystal structure revealed that the space-group symmetry is retained, but the rigid imidazolate ligand twists at its two nitrogen positions (acting as hinges), effectively reorienting to increase the SAV (Fig. 18). The change in the bulk modulus associated with such a transition has not yet been determined.

2.2.4 Theoretical studies of bulk moduli and comparison with experiments. We now discuss some of the theoretical

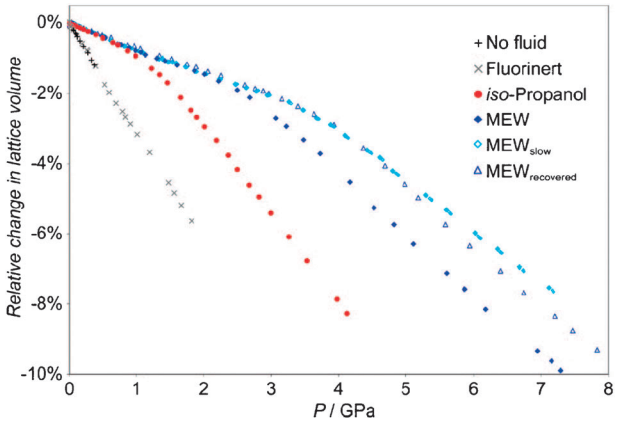

Fig. 17 The pressure-induced changes in lattice volume for the Cu-BTC framework without pressure-transmitting fluid and when pressurized by different guest molecules. Fluorinert is a non-penetrating medium. Isopropyl alcohol is a relatively large molecule compared to a mixture of methanol–ethanol–water (MEW) of 16 : 3 : 1. The "recovered" data set refers to a sample that had previously undergone a rapid decompression which had the effect of reducing the average particle size. Adapted from ref. 40 with permission, copyright (2008) American Chemical Society.

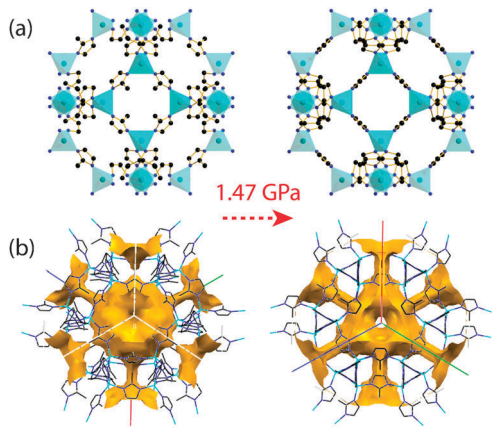

Fig. 18 Packing arrangement of ZIF-8 at ambient pressure and upon phase transition at 1.47 GPa, observe the change in the orientation of the rigid imidazolate linkers. ZnN_4 tetrahedra are represented as rigid polyhedra in (a), and the yellow surfaces denote *SAV* in (b). In particular, note the increase in size of the funnels surrounding the central nano-sized pore. H atoms are excluded for clarity. Adapted from ref. 84.

calculations for estimating the bulk modulus of hybrid framework materials. To date, only one example is available on the bulk modulus of a fully dense hybrid (*i.e.* zero *SAV*). As part of a study to understand the origin of elastic anisotropy in hybrid frameworks, Kosa *et al.*[32] also calculated the bulk modulus of ZnPA by DFT (within GGA at 0 K, Fig. 19(a)) and obtained a value of 48.6 GPa. This is markedly higher than those previously calculated for porous MOF-5 (within LDA and GGA at 0 K, K lies in the range of 16.3–18.5 GPa),[33–36] reflecting clearly that open frameworks are more compressible (Fig. 16); this is consistent with their large differential densities, *i.e.* 3.19 g cm^{-3} for ZnPA compared to 0.59 g cm^{-3} for MOF-5. On this occasion, unfortunately, experimental bulk moduli of ZnPA and MOF-5 are not available for direct comparison. Instead, comparison can be made against other materials with similar compressibilities: (i) organic molecular solids like benzene, naphthalene, anthracene and hexamine have relatively low K values in the range of 5–8 GPa,[95] (ii) ionic solids such as CsCl and NaCl have $K \approx 18$ GPa and ≈ 25 GPa, respectively,[96] while (iii) natrolite and analcime zeolites have K of 48.5 GPa and $\approx$60 GPa, respectively.[97] From Fig. 16, it appears that since the density of ZnPA is relatively high, its bulk modulus also somewhat falls into the domain corresponding to the vast majority of technical ceramic materials. There is every reason to expect a similar behavior in other dense inorganic–organic systems.

In the context of hybrid framework materials, Kosa *et al.*[32] further demonstrated that DFT could serve as a powerful tool to gain detailed insights into flexibility of the underlying building blocks. For example, in the case of ZnPA (Fig. 19(b)), the metal coordination environments (*i.e.* Zn–D_{3h}, Zn–O_h and Zn–T_d sites) were found to behave in a particularly compliant and flexible manner, whereas the stiffer building blocks are associated with the rigid organic ligands (*i.e.* C–C, C–P and

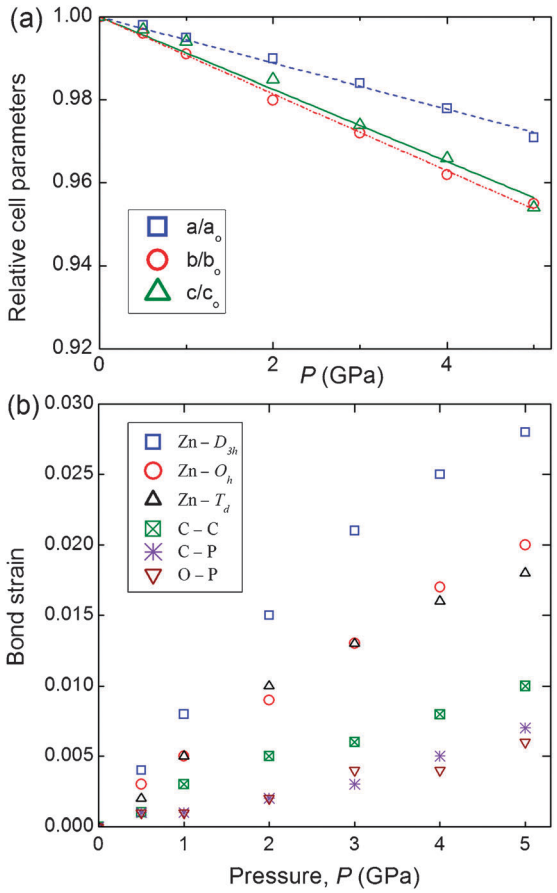

Fig. 19 DFT high-pressure predictions of ZnPA at 0 K. (a) Relative cell parameters as a function of pressure for determining the bulk modulus K. (b) Comparison between the bond strains associated with each building block given in Fig. 8(a). The symbols D_{3h}, O_h and T_d designate trigonal bipyramidal, octahedral and tetrahedral Zn coordination environments, respectively. Adapted from ref. 32.

O–P bonds found in phosphate and phosphonate groups). Such a distinct characteristic appears to be consistent with experimental observations previously made on other dense framework systems (*e.g.* ref. 30 and 31). In this respect, the application of computer simulations has enabled the development of understanding that often cannot be gained through experimental means alone.

It would be of interest to consider examples in which the bulk modulus of a MOF-type material is known both experimentally and theoretically. The first exemplar is on Cu-BTC, whereby $K \approx 30$ GPa has been measured at room temperature by means of high-pressure crystallography using a non-penetrating pressure-transmitting medium (*e.g.* Fluorinert).[40] Molecular dynamics (MD) simulations have produced reasonably good agreements; Tafipolsky *et al.*[41] have obtained a lower value of 25 GPa, while the work by Zhao *et al.*[42] estimated a higher value at 35.2 GPa. Given that both calculations were performed at 300 K, the reason behind the observed discrepancy is unclear and requires further investigations; this may well be the outcome of different force field, as has been observed in MD simulations of MOF-5 (Table 2). Like in the case of elastic stiffnesses (Fig. 10), the effects of temperature on the bulk modulus (K) of MOFs can be significant. To illustrate, finite-temperature MD simulations reported by Han and Goddard[39] clearly demonstrated a drop in the bulk modulus of MOF-5 by about 13% (from 19.4 GPa to 16.7 GPa) between the temperature range of 10 K and 300 K. In comparison, another recent study by Tafipolsky and Schmid[38] has predicted a more substantial drop in K, of up to 25%, when the simulation temperature was raised from 0 K to 300 K. Clearly, experimental data are now needed to verify the reliability of such theoretical studies.

Our second example is centered on ZIF-zni and its lightweight analogue $LiB(Im)_4$. Of which, their experimental K values are $\approx$ 14 GPa[43] and 16.6 GPa,[46] respectively. In comparison, DFT calculations (within GGA at 0 K) of the two structures correctly predicted their room-temperature experimental values (DFT results: 13.25 GPa and 16.54 GPa for ZIF-zni and $LiB(Im)_4$ respectively).[46] This is an intriguing outcome because the calculations, despite being done at 0 K, showed excellent agreement to experimental data measured at ambient conditions. Although the reason behind this is not yet clear, we anticipate that finite-temperature simulations (MD) at 300 K might predict moduli that are at least 10% to 15% lower.

2.3 Shear modulus

The shear modulus, G (*i.e.* ratio of shear stress to shear strain) is a measure of the stiffness of a material or structure when subjected to (opposing) shear forces acting parallel to the surfaces (Fig. 1(c)). G is also known as the rigidity modulus, and in the context of hybrid materials, this signifies the resistance against framework elastic distortion under the influence of shear loading.

2.3.1 Theoretical predictions. At present, our understanding of the shear modulus of open hybrid frameworks is limited to that of cubic IRMOF systems, and much of the knowledge we have stems from DFT and MD computational studies. For a single crystal of cubic symmetry, the elastic shear properties can be characterized by: (i) $G\{100\}\langle 0kl\rangle$ which corresponds to a shear in the $\{100\}$ plane and the $\langle 0kl\rangle$ direction, this is equivalent to the C_{44} elastic stiffness coefficient, and (*ii*) $G\{110\}\langle 1\bar{1}0\rangle$ for a shear in the $\{110\}$ plane and the $\langle 1\bar{1}0\rangle$ direction, as defined by the Zener's shear constant $C' = (C_{11}–C_{12})/2$. Of course, for an isotropic system such as in a polycrystalline material, the former simply reduces to $G = C_{44}$ when $C_{44} = (C_{11}–C_{12})/2$.[98]

We first focus on $G\{100\}\langle 0kl\rangle$ of MOF-5. A number of DFT calculations at 0 K (within LDA and GGA, see Table 2) have revealed C_{44} to be between 1.2–3.6 GPa. This is strikingly small in comparison to its other two independent stiffness coefficients, *i.e.* $C_{11} \approx 28$ GPa and $C_{12} \approx 11$ GPa.[33,34,36] Finite-temperature MD simulations further demonstrate that there is a dramatic decline in C_{44} as a function of temperature, from 1.8 GPa at 10 K down to about 1 GPa at 600 K (Fig. 20).[39] Theoretical studies therefore imply that MOF-5 could become unstable when acted upon by shear loading (in the $\{100\}\langle 0kl\rangle$ slip system) in response to rotations occurring at the compliant metal sites. However, in the absence of any experimental evidence, the validity and accuracy of such a prediction cannot yet be verified. Instead, presented here are the C_{44} experimental values of several familiar cubic systems just for comparison: Na (4.2 GPa), KCl (6.3 GPa), NaCl (12.7 GPa), Ge (67 GPa) and Si (80 GPa).[98,99]

We now consider the Zener's shear constant (C') of MOF-5 and its associated IRMOF structures.[39] At 300 K, their shear moduli C' lie in the range of 6–14 GPa (Fig. 20). As in the case of C_{44}, there is also a strong correlation with respect to the framework density and porosity. The trend implies that MOFs of low density (and hence of high porosity, such as MOF-C30 which has 30 aromatic carbon atoms in each linker, see Fig. 10(a)) exhibit not only relatively low shear moduli but also relatively weak temperature-dependent elastic properties. Furthermore it is important to emphasize that there exists anisotropy in the shear stiffness property of all the cubic IRMOFs considered here. For instance, in the case of MOF-5, the magnitude of C' is clearly an order of magnitude larger than that of C_{44}.

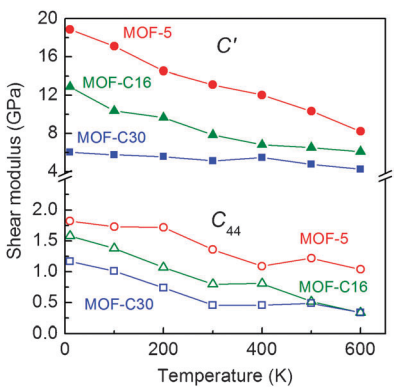

Fig. 20 Temperature-dependent shear moduli of cubic IRMOFs calculated by MD simulations.[39] The framework structures concerned are depicted in Fig. 10(a).

2.3.2 Experimental observations. The shear modulus of hybrid framework single crystals has not yet been directly measured, probably because the vast majority of existing experimental methods require the use of sizeable samples (typically of the order of 10 mm across, *e.g.* for ultrasonic techniques[58]). Brillouin scattering could be useful in this respect, and has been successfully employed to extract the elastic constants of relatively small inorganic crystals of $\approx$ 100 μm across (*e.g.* ref. 97 and 100), from which G can be derived.

On one occasion, however, it was possible to indirectly determine the shear modulus of the dense framework CuPA-2 through spherical nanoindentation[30] (Fig. 21). By identifying the first pop-in events and then applying the Hertzian elastic contact theory,[101] the critical resolved shear stress (τ_{crit}) in orientations parallel and perpendicular to the 2-D layers were obtained. It follows that for crystalline materials, since G is typically of the order of 10 τ_{crit},[102] the shear moduli parallel and perpendicular to the layers were estimated as 10–11 GPa and 7.6 GPa, respectively. These appear to be reasonable numbers in view of their much higher Young's moduli of 55–61 GPa and 34.5 GPa, respectively. Again, this study confirmed that strong directionality of the chemical bonds can give rise to shear stiffness anisotropy.

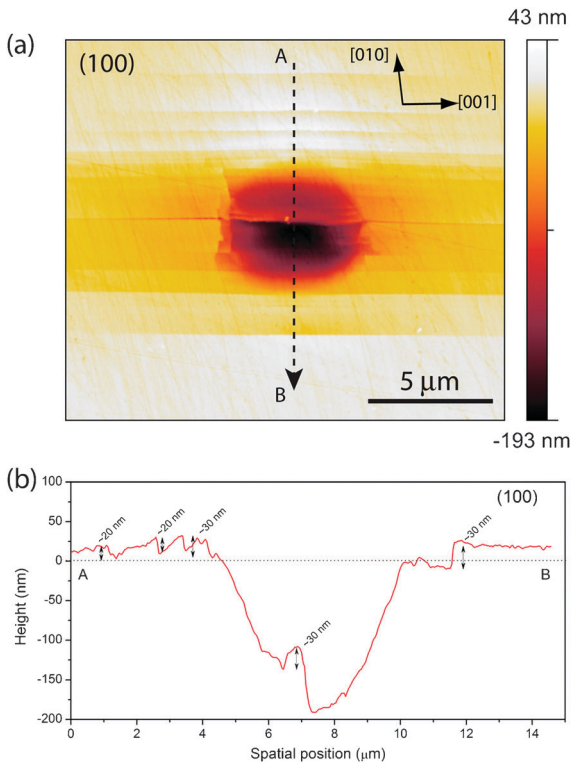

Fig. 21 AFM height topology obtained from a residual spherical indent to a maximum load of 50 mN on CuPA-2 (*i.e.* corresponds to the green curve in Fig. 26(a)). (a) shear bands formation detected on the {100}-oriented facets. (b) 2-D cross-sectional profile along A-B highlighting the slip steps developed inside the indent and around its vicinity. Adapted from ref. 30.

3. Hardness

The hardness of a material is a measure of its resistance towards permanent plastic deformation. For single crystals, thin films and monoliths of hybrid frameworks, their hardnesses can be conveniently measured using a nanoindenter. Based on the Oliver and Pharr method,[103] the hardness value (or nanohardness, $H = P/A_c$) is calculated by dividing the applied load (P) by the surface contact area developed under that load (A_c). One should recognize that hardness is not a unique material property but is a function of the test method used, the chosen test parameters (*e.g.* indenter tip geometry, applied load, indentation depth *etc.*) and the model adopted to calculate the H values. In light of this, hardness measurements obtained from different test methods are not necessarily comparable, unless the main features of the tests are similar.

3.1 Dense hybrid frameworks

First, we focus on the hardnesses of CuPA polymorphs as a function of crystal orientations, as shown in Fig. 22. Evidently, the overall hardness of CuPA-1 (H = 4.2–4.7 GPa) is approximately a factor of two greater than that of CuPA-2 (H = 2.3–2.5 GPa). As in the case of elasticity (Section 2), this finding confirms that structural dimensionality and connectivity strongly affect the framework mechanical properties. Nevertheless, in contrast to the large anisotropies observed in their Young's moduli, both polymorphs exhibit relatively weak dependence on crystallographic orientation. To illustrate, the ratio of hardnesses in CuPA-2 is given by $H_{(100)} : H_{(010)} : H_{(001)}$ = 1.00 : 1.12 : 1.04, for which the (010)-oriented facet is the hardest whereas the hardnesses parallel to the layers were found to be quite similar. Here, it is striking to see that despite its lamellar structure, the maximum change in H is only about 12% (*vs.* 77% maximum change in E, see Fig. 4).[30] Another example concerns the hardness anisotropy of cerium oxalate formate

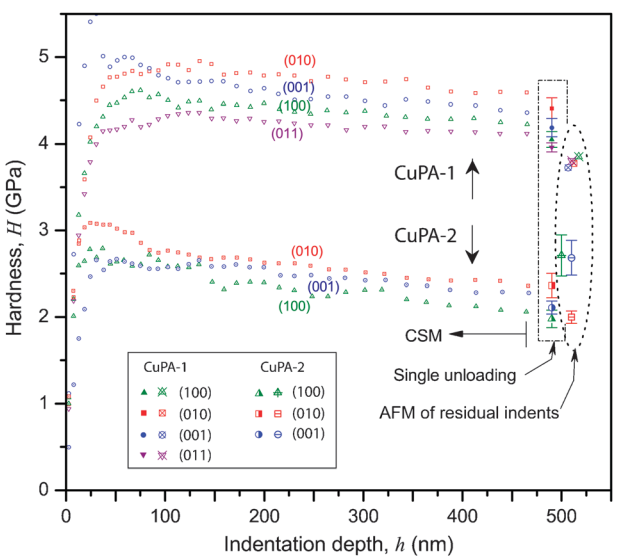

Fig. 22 Hardness of CuPA-1 and CuPA-2 polymorphs as a function of crystallographic orientation and nanoindentation test method. The CSM data represent the average values. Adapted from ref. 30.

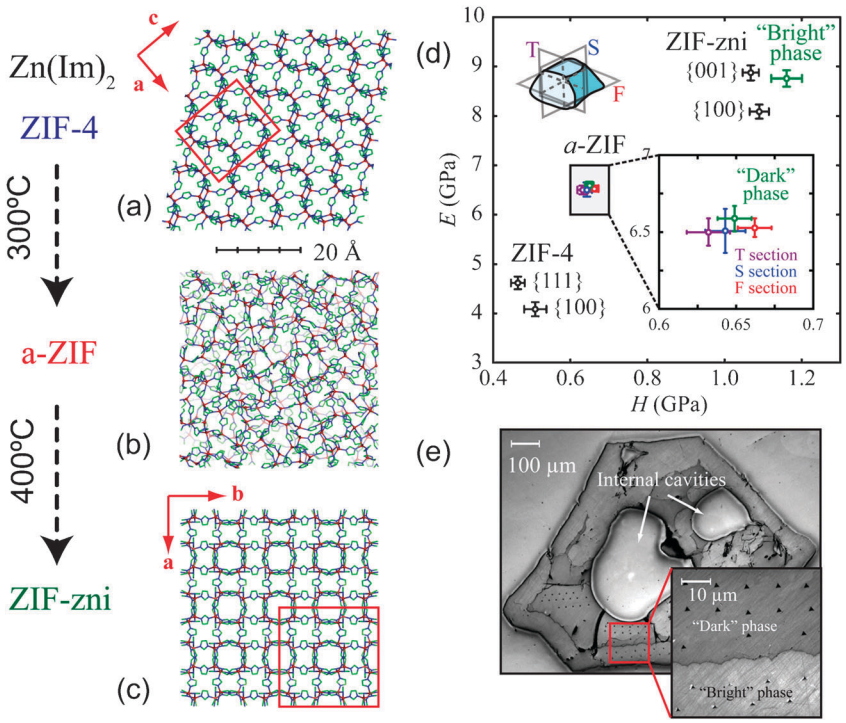

Fig. 23 (a) to (c) show the crystalline–amorphous–crystalline transition of $Zn(Im)_2$ upon heating. The red outlines denote the corresponding unit cells of the crystalline phases. (d) Young's moduli and hardnesses determined for the different phases along specific orientations, here "T", "S" and "F" refer to the transverse, sagittal, and frontal sections of the indented monolith respectively. (e) A partially recrystallized monolith consisting of *a*-ZIF ("dark") and ZIF-zni ("bright") phases. The inset shows the indentations used to distinguish the two phases and results obtained are plotted in panel (d). Adapted from ref. 45.

single crystals (Fig. 6).[31] It was found that $H_{(001)} > H_{(100)} > H_{(010)}$, whereby the (001)-oriented facet appears to be the hardest (H = 4.6 GPa). Likewise, the maximum change in its hardness is only 15%, again relatively small in comparison with an 82% change in its Young's modulus.

The seemingly small hardness anisotropy highlighted above resulted from the combinations of elastic and plastic deformation mechanisms taking place in the vicinity of the nanoindenter tip. Specifically, when indenting crystalline solids, hardness anisotropy is a clear demonstration of the complex dislocation activities occurring in the plastic zone in response to different indenter geometries used to produce the pressure.[104] Indeed, studies conducted on (metallic) single crystals[105,106] confirmed that complex stress states could develop in the small volume located under the indenter tip. When multiple slip systems are activated simultaneously to accommodate plastic flow (section 4), averaging of intrinsic hardness values therefore yields a smaller hardness anisotropy even though different crystallographic orientations are being probed.

3.2 Nanoporous hybrid frameworks

While the hardness properties of dense frameworks (reported thus far, see Fig. 2) appear to all converge in the relatively narrow range of 1–10 GPa, the hardnesses of nanoporous frameworks are considerably lower but can cover at least three orders of magnitude. Notably, MOF-5 is by far the softest framework material measured (*via* nanoindentation[36]), with hardness of just over 40 MPa; this is similar to some soft organic polymers. Such a low hardness property could result from its notably small shear modulus (C_{44}, see Fig. 20). As a consequence, the framework is weak against shear stresses generated by the indenter tip and this can lead to irreversible plastic deformation. Moreover, in view of the poor hydrothermal stability of MOF-5,[65] the small hardness value may partly be the result of framework degradation.

In terms of ZIF structures, their mechanical hardnesses have been shown to exhibit clear inverse correlation with respect to the internal accessible void space (Fig. 14(b)).[44] Highly porous frameworks of low densities such as ZIF-8, -20 and -68 are indeed relatively soft phases, with hardness values lying in the range of 200–500 MPa. As the framework turns denser, the hardness also increases accordingly. Frameworks that feature sterically bulky aromatic linkers, for instance ZIF-7 and -9, contain a markedly reduced level of porosity and can yield moderate hardnesses (H = 650–700 MPa). At present, the dense ZIF-zni phase with $H \approx 1.1$ GPa remains the hardest structure amongst the ZIF family. Its lightweight analogue $LiB(Im)_4$, conversely, is appreciably softer and the measured hardness is an order of magnitude lower ($H \approx 100$ MPa).[46] This outcome clearly parallels its low stiffness property (Fig. 15(e)) and can be ascribed to the high flexibility of LiN_4 tetrahedra. In light of this, we hypothesize that the same should be true of other lightweight Boron-Imidazolate Frameworks (BIFs) incorporating flexible linkages. It is worth emphasizing that low hardness property can generally induce large and irreversible (plastic) deformation when

the framework is mechanically loaded beyond the elastic strain. In consequence, from the mechanical viewpoint, BIF-type materials may not be as robust as their zinc analogues (*i.e.* ZIFs) for applications that push the materials beyond their elastic limits.

In a recent study, Bennett *et al.*[45] demonstrated that the porous ZIF-4 structure undergoes a crystal–amorphous transition (Fig. 23) on heating to 300 °C to yield an amorphous phase, termed *a*-ZIF. This glass-like phase is recoverable to ambient conditions or may be converted into the crystalline ZIF-zni phase by further heating to 400 °C. Similar amorphization mechanisms are expected in other MOFs. Neutron total scattering experiment indicated that the structure of *a*-ZIF is best understood as a continuous random network structure akin to amorphous SiO_2 (Fig. 23(b)). Nanoindentation was used to confirm the loss of anisotropy in the amorphous phase (Fig. 23(d)). The results clearly demonstrate that the hardness and Young's modulus of *a*-ZIF ($H \approx 0.65$ GPa, $E \approx 6.5$ GPa) to be intermediate between, but distinct from, those of crystalline ZIF-zni and ZIF-4. This study suggests that glass-like MOFs could offer a number of exciting opportunities in the development of functional amorphous materials; for example, the preparation of electroluminescent glasses for advanced photonics would likely benefit from their isotropic mechanical properties.

4. Plasticity

In the context of functional materials like hybrid frameworks, permanent shape change and local structural distortion caused by irreversible plastic deformation can seriously impair their functional performance. However, unlike ductile materials (*e.g.* metals) that can undergo extensive plastic deformation, plasticity in hybrid frameworks is bound to be limited (at ambient conditions) due to strong directional bonding. In the complete absence of plasticity, brittle fracture ensues once the elastic limit is exceeded.

4.1 Onset of plasticity

The plastic deformation behavior pertaining to (small) single crystals of hybrid frameworks can best be investigated *via* spherical nanoindentation. A spherical diamond tip (nominal radius of the order of 1 μm) can establish a larger areal contact at small penetration depths (*vs.* a Berkovich tip), hence useful for delaying the onset of plasticity.[107] Also by exploiting its capability to generate changing contact strain as a function of indentation depth, indentation stress–strain curves can be derived, from which the elastic limit can be estimated.

The method described above has been used to investigate the elastic-plastic transition of cerium oxalate formate.[31] In Fig. 24(a), the indentation yield pressure (P_y) denotes the critical stress corresponding to the onset of plastic deformation, that is the point of deviation from Hookean linearity. Although P_y can be thought of as equivalent to the yield strength in the traditional sense, their absolute values are generally not identical.[108] Here, the (001)-oriented facet exhibits the highest yield pressure ($P_y \approx 2$ GPa), while those corresponding to the (100)- and (010)-oriented planes are relatively lower at about 1.4 GPa and 1.2 GPa, respectively. In consequence, the yielding response as a function of the crystallographic orientation can be ranked as $P_{y(001)} > P_{y(100)} > P_{y(010)}$, which obeys Tabor's relationship $H = C \cdot P_y$.[109] The hardness is therefore proportional to the yield pressure, and the constraint factor C varies with the crystal facet because of anisotropy.

4.2 Deformation mechanisms

The shape of the stress–strain curves (Fig. 24(a) inset) provides indications on the type of strain-hardening behavior that dominates in each crystallographic orientation. In this lanthanide mixed-ligand compound, the (001)-oriented plane appears to obey a power-law hardening behavior (*e.g.* of the form $P_m \propto (a/R)^n$, where n is the strain exponent) generally associated with dislocation entanglement. In contrast, the (100)-oriented plane shows a somewhat perfectly plastic response, with a plateau of close to 2 GPa. Atomic force microscopy (AFM) height topology (Fig. 25) shows that the different strain hardening behavior can also be correlated

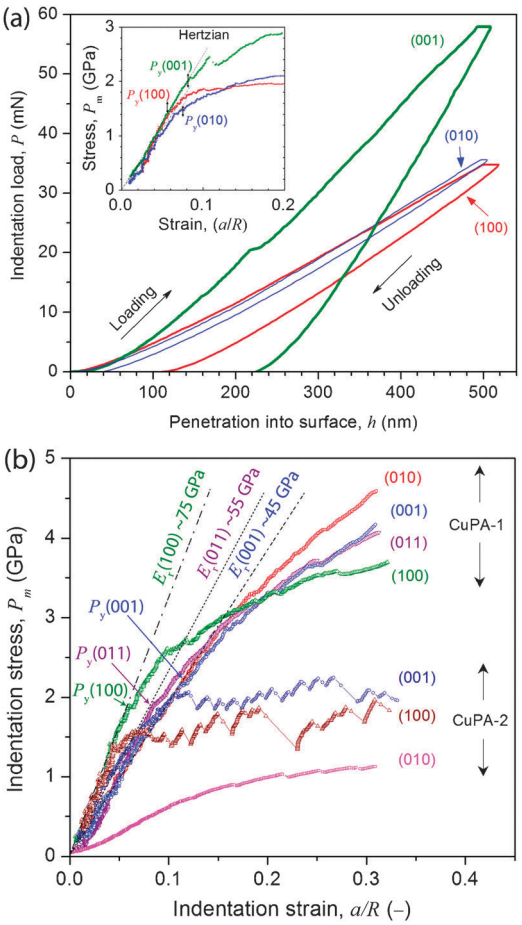

Fig. 24 (a) Typical load-displacement curves obtained from spherical nanoindentation of cerium oxalate formate single crystals. The inset depicts the indentation stress–strain curves derived for the different crystal orientations, whereby P_y designates the transition from purely elastic to plastic deformation. (b) Indentation stress–strain curves of CuPA polymorphs (E_r is the reduced modulus[52]). The straight lines denote the purely elastic Hertzian contact. Note that the abrupt drops in stresses observed in the (001)- and (100)-oriented planes of CuPA-2 are attributed to "pop-in" phenomena (see Fig. 26(a)). Panel (a) is adapted from ref. 31 and panel (b) is from ref. 30.

to the extent of pile-up developed around the residual indents. To further elucidate the underlying plasticity mechanisms, however, transmission electron microscopy (TEM) examinations are warranted to confirm the presence of dislocation activities needed to accommodate plastic flow. For example, TEM studies on several "brittle" inorganic systems have revealed twinning and dislocation glide mechanisms to be active beneath micron-sized indents.[110–112]

The same nanoindentation procedure was applied to examine the plastic deformation behavior surrounding copper phosphonoacetate single crystals (Fig. 24(b)).[30] Between the two polymorphs, crystal planes in CuPA-1 exhibit higher yield pressures ($P_y \approx 1.8$–2.3 GPa) and demonstrate strain-hardening like characteristics in the plastic regime ($C \approx 2$–2.4). The yield pressures of CuPA-2 ($P_y \approx 0.7$–1.9 GPa) are smaller than those of the former. Their constraint factors are lower along the directions of the 2-D layers ($C \approx 1.2$–1.5), but higher by a factor of two in the orientation normal to the layers ($C \approx 3.6$). In comparison to conventional materials, we note that a C value of about 1.5 is commonly associated with "brittle" materials (*e.g.* ceramics and glasses), whereas $C \approx 3$ is typical of "ductile" behavior characteristic of metallic materials.[113]

Plastic deformation mechanism in orientations parallel to the layers in CuPA-2 is characterized by the formation of slip steps or shear bands, as shown in Fig. 21. The height of the slip steps can range from about 10 nm to 50 nm, which is consistent with the size of the pop-ins (*i.e.* abrupt displacements of the nanoindenter at constant load). Given that all steps are prevalent along the ⟨001⟩-oriented axis, this confirms their formation to be associated with the breakage of hydrogen bonds. It follows that the small C values of the

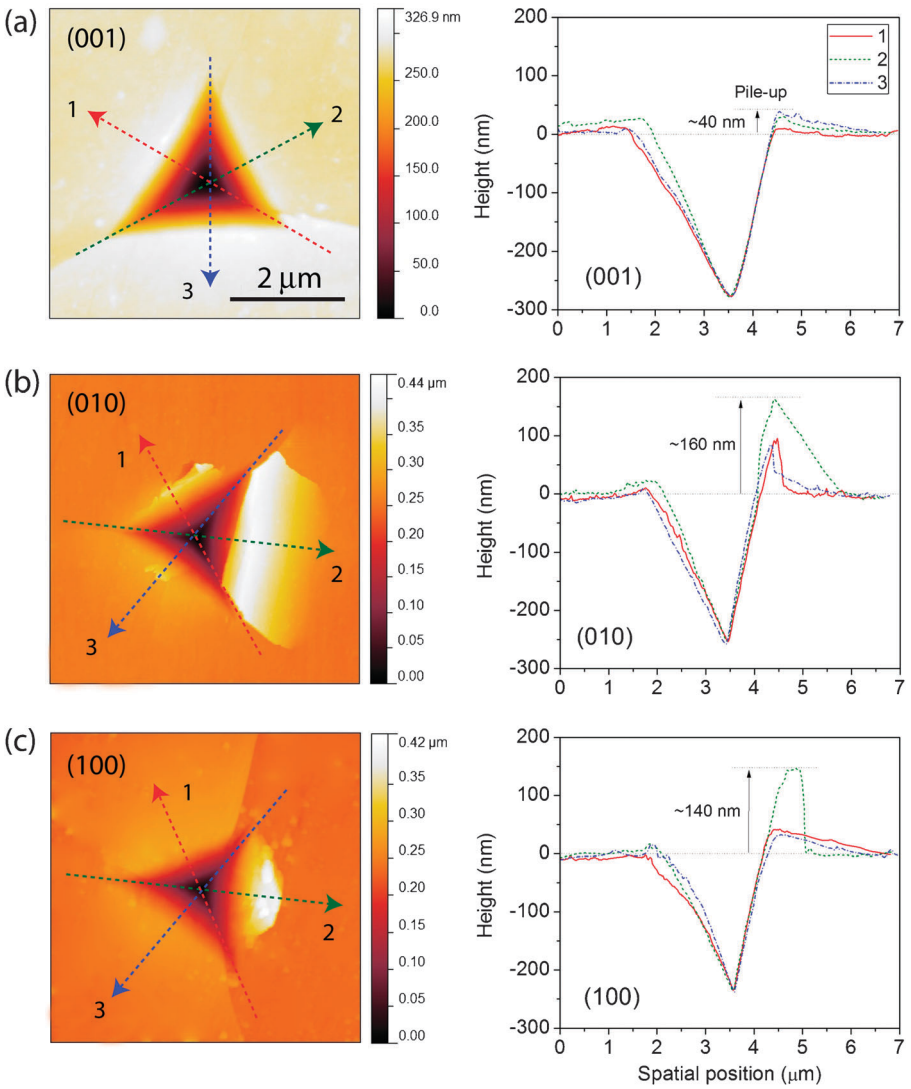

Fig. 25 AFM height topologies of residual Berkovich indents made on the three orthogonal crystal faces of cerium oxalate formate. The cross-sectional profiles on the right correspond to the three designated directions indicated by the red, green and blue arrows respectively. Note that the shape of the pile-up developed around the indent is strongly correlated to the orientation of the crystal facet, which suggests different strain hardening behavior. (a) The (001)-oriented facet exhibits the least amount of pile-up since it can undergo extensive strain hardening in the plastic regime (Fig. 24(a) inset). In contrast, (b) and (c) confirm that the (100)- and (010)-oriented planes that undergo elastic-perfectly plastic deformation tend to demonstrate more pile-ups, ranging from 50–150 nm. Right panels adapted from ref. 31.

(001)- and (100)-oriented facets are indicative of brittle mechanical behavior.

4.3 Viscoplasticity

Closer examination reveals that the higher C value measured along the (010)-oriented facets of CuPA-2 is associated with visco-plastic phenomena. Fig. 26 clearly shows time-dependent plasticity within the hold segment $\alpha \rightarrow \beta$, signifying a creep-like deformation to be operational under constant load. Significantly, creep can occur below the framework yield pressure (P_y). The displacement rate (dh/dt) of the (010) face at the maximum load was found to be $\approx$8.6 nm s^{-1}, close to two orders of magnitude higher than those measured for the (001)- and (100)-oriented facets ($dh/dt \approx 0.1$ nm s^{-1}). For this particular 2-D framework, the strongly anisotropic creep behavior evidently results from the directionality of interlayer hydrogen bonding. Likewise, creep deformation has also been observed in MOF-5,[36] but the underlying mechanism has not yet been elucidated for a nanoporous hybrid framework.

5. Fracture toughness

The fracture toughness (K_c) of a material is a measure of its resistance against crack propagation leading to fracture. It is an important mechanical property for all load-bearing technological devices because failure by crack propagation can often occur at stress levels well below the material yield strength.[114]

Thus far, there is only one attempt to characterize the fracture toughness of hybrid framework materials. The study was done on dense CuPA frameworks by nanoindentation, wherein K_c of different crystal facets was estimated by means of radial cracks emanating from the Berkovich indents.[31] The K_c of CuPA-1 was reported to be in the range of 0.10–0.33 MPa $m^{1/2}$, whereas in CuPA-2 it lies within 0.08–0.12 MPa $m^{1/2}$. The former exhibits higher toughness values and greater than that of the latter by as much as a factor of four in certain orientations. Reducing the network connectivity and dimensionality appears to have an adverse impact on the overall framework toughness. In particular, we note that the fracture toughness of CuPA is approaching the lower bound typically associated with brittle materials. To illustrate, presented here are the K_c values of a selection of inorganic materials: $BaTiO_3$ (0.7 MPa $m^{1/2}$),[115] quartz (1.5 MPa $m^{1/2}$),[116] alumina (4 MPa $m^{1/2}$) and zirconia (10 MPa $m^{1/2}$).[117] Interestingly, fracture toughness studies[118,119] on organosilicate hybrid coatings (*NB*: these are not crystalline frameworks) have reported values in the range of 0.14–0.23 MPa $m^{1/2}$, which indeed resemble those found in CuPA.

It is possible to establish connections between the subsurface fracture morphology and the underlying crystalline structure. For example, on the (100) facet of CuPA-1 (Fig. 27(a–b)), four radial cracks propagated in the ⟨011⟩ directions, independent of indenter geometry. Referring to Fig. 3(a), one can rationalize that they correspond the (011) and ($0\bar{1}1$) planes, and such cracks are likely to initiate from the rupture of adjacent carboxylate headgroups linking the quasi-inorganic chains. In the case of CuPA-2, an interesting crack pattern can be observed on the (010) plane (Fig. 27(c)), indicative of its underlying layered structure being susceptible to creep

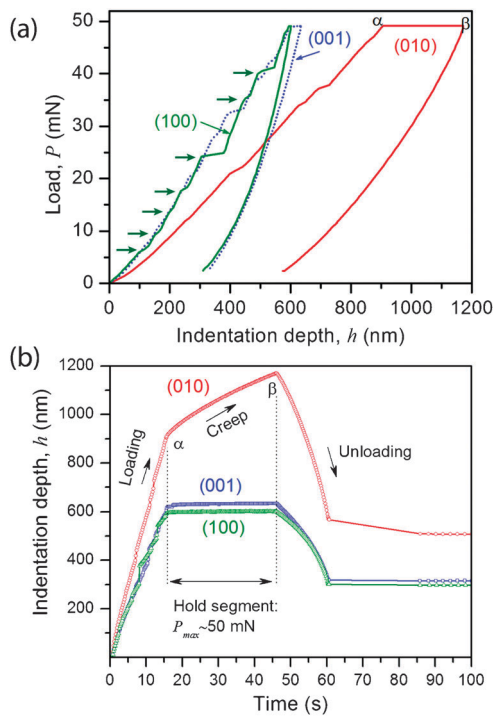

Fig. 26 (a) Representative spherical nanoindentation curves of the crystal faces of CuPA-2. The maximum loads were 50 mN with a hold time of 30 s prior to unloading. The horizontal arrows indicate the displacement bursts or "pop-ins" that are typically associated with plastic deformation. (b) The indentation depth *versus* time curves that correspond to the data presented in (a), in which extensive creep deformation is indicated by the segment designated by $\alpha \rightarrow \beta$, detected only on the (010) facet. Adapted from ref. 30.

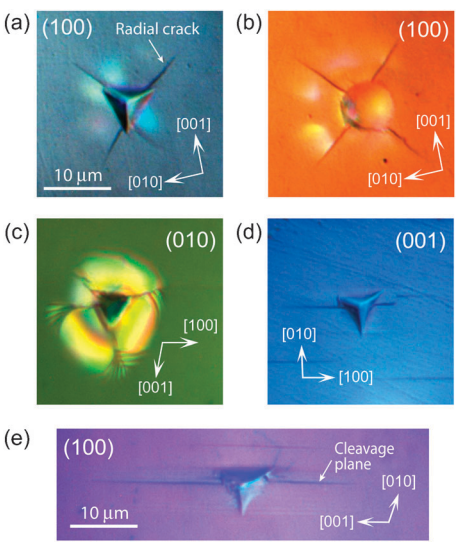

Fig. 27 Interference contrast optical micrographs showing the fracture morphology on the main crystal facets of (a–b) CuPA-1 and (c–e) CuPA-2. A combination of radial and/or lateral cracks can be observed, while closely-spaced fringes indicate a steeper inclination in panel (c). Adapted from ref. 30.

deformation under compressive loading. By contrast, (001)- and (100)-oriented facets (Fig. 27(d–e)) developed only unidirectional cracks propagating parallel to the planar axis of the layers, but with no cracks forming in the transverse directions. Clearly, these originated from the rupture of hydrogen bonds whereby the {010} planes correspond to the cleavage planes.

Very little has been reported on the fracture toughness of nanoporous hybrid frameworks, apart from some qualitative observations indicating a somewhat tougher response due to their open framework architectures.[36,44] Evidently, the fracture behavior of hybrid frameworks is another key area that warrants further investigations.

6. Summary and perspectives

The purpose of this critical review is to not only illustrate the progress that has been made in many fundamental aspects pertaining to the mechanical behavior of hybrid framework materials, but also to encourage more intensive research in this direction. Interestingly, although the hybrid framework area has now sustained tremendous growth for nearly two decades, our discussion in the preceding sections encompass only reports that have emerged in the last 5 years since there was virtually no activity in this topic before then. Whilst there has been work concerning the ferroelectric and ferromagnetic properties of hybrid frameworks (*e.g.* ref. 24, 120 and 121), there is not yet any report on piezoelectricity for which the elasticity of the framework shall be strongly correlated to its piezoelectric behavior.

The need to improve our understanding of the mechanical properties of this new class of solid-state materials is self-evident. Their successful implementation in real-world technological applications necessitates detailed knowledge in addition to careful optimization of a broad range of mechanical properties, some of which have been highlighted in the above discussion. In terms of materials optimization, we are fortunate that the immensely vast chemical and structural diversity of hybrids means there are endless avenues for designing new materials to target specific uses. The challenge now, however, lies in establishing and controlling the complex structure–property relationships that incorporate both functional and mechanical characteristics.

Acknowledgements

We thank the University of Cambridge and the European Research Council for providing financial support. JCT is particularly grateful to Dr Monica Kosa and Dr A. Thirumurugan for a number of productive scientific discussions.

References

1 A. K. Cheetham, C. N. R. Rao and R. K. Feller, *Chem. Commun.*, 2006, 4780–4795.
2 A. K. Cheetham and C. N. R. Rao, *Science*, 2007, **318**, 58–59.
3 D. Eder, *Chem. Rev.*, 2010, **110**, 1348–1385.
4 P. M. Ajayan, L. S. Schadler, P. V. Braun and P. Keblinski, *Nanocomposite Science and Technology*, Wiley-VCH Verlag GmbH & Co. KGaA, 2nd edn, 2008.
5 *Bio-inorganic Hybrid Nanomaterials—Strategies, Syntheses, Characterization and Applications*, Wiley-VCH Verlag GmbH & Co. KGaA, 2nd edn, 2008.
6 J. S. Moya, S. Lopez-Esteban and C. Pecharroman, *Prog. Mater. Sci.*, 2007, **52**, 1017–1090.
7 S. Mohnani and D. Bonifazi, *Coord. Chem. Rev.*, 2010, **254**, 2342–2362.
8 A. K. Cheetham, G. Férey and T. Loiseau, *Angew. Chem., Int. Ed.*, 1999, **38**, 3268–3292.
9 M. J. Rosseinsky, *Microporous Mesoporous Mater.*, 2004, **73**, 15–30.
10 S. Kitagawa, R. Kitaura and S. Noro, *Angew. Chem., Int. Ed.*, 2004, **43**, 2334–2375.
11 G. Férey, *Chem. Soc. Rev.*, 2008, **37**, 191–214.
12 O. M. Yaghi, M. O'Keeffe, N. W. Ockwig, H. K. Chae, M. Eddaoudi and J. Kim, *Nature*, 2003, **423**, 705–714.
13 C. N. R. Rao, S. Natarajan and R. Vaidhyanathan, *Angew. Chem., Int. Ed.*, 2004, **43**, 1466–1496.
14 *Themed issue*: *Metal-organic frameworks*, *Chem. Soc. Rev.*, 2009, **38**, 1201–1508.
15 R. E. Morris and P. S. Wheatley, *Angew. Chem., Int. Ed.*, 2008, **47**, 4966–4981.
16 L. J. Murray, M. Dinca and J. R. Long, *Chem. Soc. Rev.*, 2009, **38**, 1294–1314.
17 R. Q. Zou, A. I. Abdel-Fattah, H. W. Xu, Y. S. Zhao and D. D. Hickmott, *CrystEngComm*, 2010, **12**, 1337–1353.
18 J. Lee, O. K. Farha, J. Roberts, K. A. Scheidt, S. T. Nguyen and J. T. Hupp, *Chem. Soc. Rev.*, 2009, **38**, 1450–1459.
19 L. Q. Ma, C. Abney and W. B. Lin, *Chem. Soc. Rev.*, 2009, **38**, 1248–1256.
20 P. Horcajada, C. Serre, M. Vallet-Regi, M. Sebban, F. Taulelle and G. Férey, *Angew. Chem., Int. Ed.*, 2006, **45**, 5974–5978.
21 A. C. McKinlay, R. E. Morris, P. Horcajada, G. Férey, R. Gref, P. Couvreur and C. Serre, *Angew. Chem., Int. Ed.*, 2010, **49**, 6260–6266.
22 S. Horike, S. Shimomura and S. Kitagawa, *Nat. Chem.*, 2009, **1**, 695–704.
23 C. N. R. Rao, A. K. Cheetham and A. Thirumurugan, *J. Phys.: Condens. Matter*, 2008, **20**, 083202.
24 P. Jain, N. S. Dalal, B. H. Toby, H. W. Kroto and A. K. Cheetham, *J. Am. Chem. Soc.*, 2008, **130**, 10450–10451.
25 K. W. Chapman, G. J. Halder and P. J. Chupas, *J. Am. Chem. Soc.*, 2009, **131**, 17546–17547.
26 M. D. Allendorf, R. J. T. Houk, L. Andruszkiewicz, A. A. Talin, J. Pikarsky, A. Choudhury, K. A. Gall and P. J. Hesketh, *J. Am. Chem. Soc.*, 2008, **130**, 14404–14405.
27 D. Zacher, O. Shekhah, C. Woll and R. A. Fischer, *Chem. Soc. Rev.*, 2009, **38**, 1418–1429.
28 R. Ameloot, L. Stappers, J. Fransaer, L. Alaerts, B. F. Sels and D. E. De Vos, *Chem. Mater.*, 2009, **21**, 2580–2582.
29 A. S. Huang, H. Bux, F. Steinbach and J. Caro, *Angew. Chem., Int. Ed.*, 2010, **49**, 4958–4961.
30 J. C. Tan, C. A. Merrill, J. B. Orton and A. K. Cheetham, *Acta Mater.*, 2009, **57**, 3481–3496.
31 J. C. Tan, J. D. Furman and A. K. Cheetham, *J. Am. Chem. Soc.*, 2009, **131**, 14252–14254.
32 M. Kosa, J. C. Tan, C. A. Merrill, M. Krack, A. K. Cheetham and M. Parrinello, *ChemPhysChem*, 2010, **11**, 2332–2336.
33 W. Zhou and T. Yildirim, *Phys. Rev. B: Condens. Matter Mater. Phys.*, 2006, **74**, 180301.
34 A. Samanta, T. Furuta and J. Li, *J. Chem. Phys.*, 2006, **125**, 084714.
35 M. Mattesini, J. M. Soler and F. Yndurain, *Phys. Rev. B: Condens. Matter Mater. Phys.*, 2006, **73**, 094111.
36 D. F. Bahr, J. A. Reid, W. M. Mook, C. A. Bauer, R. Stumpf, A. J. Skulan, N. R. Moody, B. A. Simmons, M. M. Shindel and M. D. Allendorf, *Phys. Rev. B: Condens. Matter Mater. Phys.*, 2007, **76**, 184106.
37 J. A. Greathouse and M. D. Allendorf, *J. Phys. Chem. C*, 2008, **112**, 5795–5802.
38 M. Tafipolsky and R. Schmid, *J. Phys. Chem. C*, 2009, **113**, 1341–1352.
39 S. S. Han and W. A. Goddard, *J. Phys. Chem. C*, 2007, **111**, 15185–15191.

40 K. W. Chapman, G. J. Halder and P. J. Chupas, *J. Am. Chem. Soc.*, 2008, **130**, 10524–10526.
41 M. Tafipolsky, S. Amirjalayer and R. Schmid, *J. Phys. Chem. C*, 2010, **114**, 14402–14409.
42 L. Zhao, Q. Yang, Q. Ma, C. Zhong, J. Mi and D. Liu, *J. Mol. Model.*, 2010, DOI: 10.1007/s00894-00010-00720-x, in press.
43 E. C. Spencer, R. J. Angel, N. L. Ross, B. E. Hanson and J. A. K. Howard, *J. Am. Chem. Soc.*, 2009, **131**, 4022–4026.
44 J. C. Tan, T. D. Bennett and A. K. Cheetham, *Proc. Natl. Acad. Sci. U. S. A.*, 2010, **107**, 9938–9943.
45 T. D. Bennett, A. L. Goodwin, M. T. Dove, D. A. Keen, M. G. Tucker, E. R. Barney, A. K. Soper, E. G. Bithell, J. C. Tan and A. K. Cheetham, *Phys. Rev. Lett.*, 2010, **104**, 115503.
46 T. D. Bennett, J. C. Tan, S. A. Moggach, R. Galvelis, C. Mellot-Draznieks, B. A. Reisner, A. Thirumurugan, D. R. Allan and A. K. Cheetham, *Chem.–Eur. J.*, 2010, **16**, 10684–10690.
47 A. Demessence, P. Horcajada, C. Serre, C. Boissiere, D. Grosso, C. Sanchez and G. Férey, *Chem. Commun.*, 2009, 7149–7151.
48 J. C. Tan and A. K. Cheetham, *Unpublished data obtained from single-crystal nanoindentation experiments*, 2010.
49 R. Robson, *J. Chem. Soc., Dalton Trans.*, 2000, 3735–3744.
50 R. Robson, *Dalton Trans.*, 2008, 5113–5131.
51 A. Gouldstone, N. Chollacoop, M. Dao, J. Li, A. M. Minor and Y. L. Shen, *Acta Mater.*, 2007, **55**, 4015–4039.
52 W. C. Oliver and G. M. Pharr, *J. Mater. Res.*, 2004, **19**, 3–20.
53 J. J. Vlassak and W. D. Nix, *J. Mech. Phys. Solids*, 1994, **42**, 1223–1245.
54 J. C. Hay, E. Y. Sun, G. M. Pharr, P. F. Becher and K. B. Alexander, *J. Am. Ceram. Soc.*, 1998, **81**, 2661–2669.
55 *Hybrid Materials: Synthesis, Characterization, and Applications*, Wiley-VCH Verlag GmbH & Co. KGaA, 2007.
56 O. L. Blakslee, *J. Appl. Phys.*, 1970, **41**, 3373–3382.
57 S. Romero, A. Mosset and J. C. Trombe, *J. Solid State Chem.*, 1996, **127**, 256–266.
58 J. D. Bauer, E. Haussuhl, B. Winkler, D. Arbeck, V. Milman and S. Robertson, *Cryst. Growth Des.*, 2010, **10**, 3132–3140.
59 F. M. Capaldi, M. C. Boyce and G. C. Rutledge, *J. Chem. Phys.*, 2006, **124**, 214709.
60 A. Janotti, D. Segev and C. G. Van de Walle, *Phys. Rev. B: Condens. Matter Mater. Phys.*, 2006, **74**, 045202.
61 A. J. Cohen, P. Mori-Sanchez and W. T. Yang, *Science*, 2008, **321**, 792–794.
62 S. Kummel and L. Kronik, *Rev. Mod. Phys.*, 2008, **80**, 3–60.
63 H. Li, M. Eddaoudi, M. O'Keeffe and O. M. Yaghi, *Nature*, 1999, **402**, 276–279.
64 S. S. Kaye, A. Dailly, O. M. Yaghi and J. R. Long, *J. Am. Chem. Soc.*, 2007, **129**, 14176–14177.
65 J. J. Low, A. I. Benin, P. Jakubczak, J. F. Abrahamian, S. A. Faheem and R. R. Willis, *J. Am. Chem. Soc.*, 2009, **131**, 15834–15842.
66 S. S. Han, S. H. Choi and A. C. T. van Duin, *Chem. Commun.*, 2010, **46**, 5713–5715.
67 P. Gopal and N. A. Spaldin, *Phys. Rev. B: Condens. Matter Mater. Phys.*, 2006, **74**, 538–542.
68 S. Saib and N. Bouarissa, *Phys. Status Solidi B*, 2007, **244**, 1063–1069.
69 M. Kalay, H. H. Kart, S. O. Kart and T. Cagin, *J. Alloys Compd.*, 2009, **484**, 431–438.
70 M. Eddaoudi, J. Kim, N. Rosi, D. Vodak, J. Wachter, M. O'Keeffe and O. M. Yaghi, *Science*, 2002, **295**, 469–472.
71 M. E. Ashby, A. Evans, N. A. Fleck, L. J. Gibson, H. J. W. and H. N. G. Wadley, *Metal Foams: A Design Guide*, Butterworth-Heinemann, Boston, 2000.
72 K. S. Park, Z. Ni, A. P. Cote, J. Y. Choi, R. D. Huang, F. J. Uribe-Romo, H. K. Chae, M. O'Keeffe and O. M. Yaghi, *Proc. Natl. Acad. Sci. U. S. A.*, 2006, **103**, 10186–10191.
73 Y. Q. Tian, C. X. Cai, X. M. Ren, C. Y. Duan, Y. Xu, S. Gao and X. Z. You, *Chem.–Eur. J.*, 2003, **9**, 5673–5685.
74 X. C. Huang, Y. Y. Lin, J. P. Zhang and X. M. Chen, *Angew. Chem., Int. Ed.*, 2006, **45**, 1557–1559.
75 A. Phan, C. J. Doonan, F. J. Uribe-Romo, C. B. Knobler, M. O'Keeffe and O. M. Yaghi, *Acc. Chem. Res.*, 2010, **43**, 58–67.
76 R. Banerjee, A. Phan, B. Wang, C. Knobler, H. Furukawa, M. O'Keeffe and O. M. Yaghi, *Science*, 2008, **319**, 939–943.
77 A. U. Czaja, N. Trukhan and U. Muller, *Chem. Soc. Rev.*, 2009, **38**, 1284–1293.
78 R. Banerjee, H. Furukawa, D. Britt, C. Knobler, M. O'Keeffe and O. M. Yaghi, *J. Am. Chem. Soc.*, 2009, **131**, 3875–3877.
79 R. Lehnert and F. Seel, *Z. Anorg. Allg. Chem.*, 1980, **464**, 187–194.
80 D. W. Lewis, A. R. Ruiz-Salvador, A. Gomez, L. M. Rodriguez-Albelo, F. X. Coudert, B. Slater, A. K. Cheetham and C. Mellot-Draznieks, *CrystEngComm*, 2009, **11**, 2272–2276.
81 I. A. Baburin, S. Leoni and G. Seifert, *J. Phys. Chem. C*, 2008, **112**, 9437–9443.
82 B. Wang, A. P. Cote, H. Furukawa, M. O'Keeffe and O. M. Yaghi, *Nature*, 2008, **453**, 207–212.
83 Y. Q. Tian, Y. M. Zhao, Z. X. Chen, G. N. Zhang, L. H. Weng and D. Y. Zhao, *Chem.–Eur. J.*, 2007, **13**, 4146–4154.
84 S. A. Moggach, T. D. Bennett and A. K. Cheetham, *Angew. Chem., Int. Ed.*, 2009, **48**, 7087–7089.
85 H. Zhang, T. Wu, C. Zhou, S. M. Chen, P. Y. Feng and X. H. Bu, *Angew. Chem., Int. Ed.*, 2009, **48**, 2542–2545.
86 T. Wu, J. Zhang, C. Zhou, L. Wang, X. H. Bu and P. Y. Feng, *J. Am. Chem. Soc.*, 2009, **131**, 6111–6113.
87 R. P. Liferovich, A. J. Locock, R. H. Mitchell and A. K. Shpachenko, *Can. Mineral.*, 2006, **44**, 533–546.
88 B. L. Chen, C. D. Liang, J. Yang, D. S. Contreras, Y. L. Clancy, E. B. Lobkovsky, O. M. Yaghi and S. Dai, *Angew. Chem., Int. Ed.*, 2006, **45**, 1390–1393.
89 D. N. Dybtsev, H. Chun and K. Kim, *Angew. Chem., Int. Ed.*, 2004, **43**, 5033–5036.
90 C. Serre, C. Mellot-Draznieks, S. Surble, N. Audebrand, Y. Filinchuk and G. Férey, *Science*, 2007, **315**, 1828–1831.
91 C. Boissiere, D. Grosso, S. Lepoutre, L. Nicole, A. B. Bruneau and C. Sanchez, *Langmuir*, 2005, **21**, 12362–12371.
92 Y. Raichman, M. Kazakevich, E. Rabkin and Y. Tsur, *Adv. Mater.*, 2006, **18**, 2028–2030.
93 F. Birch, *J. Geophys. Res.*, 1952, **57**, 227–286.
94 S. S. Y. Chui, S. M. F. Lo, J. P. H. Charmant, A. G. Orpen and I. D. Williams, *Science*, 1999, **283**, 1148–1150.
95 R. J. Roberts, R. C. Rowe and P. York, *Powder Technol.*, 1991, **65**, 139–146.
96 D. L. Decker, *J. Appl. Phys.*, 1971, **42**, 3239.
97 C. Sanchez-Valle, S. V. Sinogeikin, Z. A. D. Lethbridge, R. I. Walton, C. W. Smith, K. E. Evans and J. D. Bass, *J. Appl. Phys.*, 2005, **98**, 053508.
98 G. Grimvall, *Thermophysical Properties of Materials*, Elsevier Science B.V., Amsterdam, 1999.
99 R. E. Newnham, *Properties of Materials—Anisotropy, Symmetry, Structure*, Oxford University Press, Oxford, 2005.
100 L. G. Liu, C. C. Chen, C. C. Lin and Y. J. Yang, *Phys. Chem. Miner.*, 2005, **32**, 97–102.
101 K. L. Johnson, *Contact Mechanics*, Cambridge Univ. Press, Cambridge, 1985.
102 G. E. Dieter, *Mechanical Metallurgy*, McGraw-Hill, New York, 1986.
103 W. C. Oliver and G. M. Pharr, *J. Mater. Res.*, 1992, **7**, 1564–1583.
104 I. J. McColm, *Ceramic Hardness*, Plenum Publishing Corp., New York, 1990.
105 M. Rester, C. Motz and R. Pippan, *Acta Mater.*, 2007, **55**, 6427–6435.
106 N. Zaafarani, D. Raabe, R. N. Singh, F. Roters and S. Zaefferer, *Acta Mater.*, 2006, **54**, 1863–1876.
107 M. V. Swain, *Mater. Sci. Eng., A*, 1998, **253**, 160–166.
108 E. G. Herbert, W. C. Oliver and G. M. Pharr, *Philosophical Magazine*, 2006, **86**, 5521–5539.
109 D. Tabor, *The Hardness of Metals*, Clarendon Press, Oxford, 1951.
110 S. J. Lloyd, A. Castellero, F. Giuliani, Y. Long, K. K. McLaughlin, J. M. Molina-Aldareguia, N. A. Stelmashenko, L. J. Vandeperre and W. J. Clegg, *Proc. R. Soc. London, Ser. A*, 2005, **461**, 2521–2543.
111 J. E. Bradby, J. S. Williams, J. Wong-Leung, M. V. Swain and P. Munroe, *Appl. Phys. Lett.*, 2001, **78**, 3235–3237.
112 P. Mogilevsky, *Philosophical Magazine*, 2005, **85**, 3511–3539.
113 A. C. Fisher-Cripps, *Nanoindentation*, Springer, New York, 2nd edn, 2004.
114 M. E. Launey and R. O. Ritchie, *Adv. Mater.*, 2009, **21**, 2103–2110.

115 F. Meschke, O. Raddatz, A. Kolleck and G. A. Schneider, *J. Am. Ceram. Soc.*, 2000, **83**, 353–361.
116 D. L. Whitney, M. Broz and R. F. Cook, *Am. Mineral.*, 2007, **92**, 281–288.
117 J. Rosler, H. Harders and M. Baker, *Mechanical Behaviour of Engineering Materials*, Springer-Verlag, Berlin, 2007.
118 J. Malzbender, G. de With and J. M. J. den Toonder, *Thin Solid Films*, 2000, **366**, 139–149.
119 B. R. Kim and M. J. Ko, *Thin Solid Films*, 2009, **517**, 3216–3221.
120 P. Jain, V. Ramachandran, R. J. Clark, H. D. Zhou, B. H. Toby, N. S. Dalal, H. W. Kroto and A. K. Cheetham, *J. Am. Chem. Soc.*, 2009, **131**, 13625–13627.
121 M. Kurmoo, *Chem. Soc. Rev.*, 2009, **38**, 1353–1379.
122 C. M. Reddy, R. C. Gundakaram, S. Basavoju, M. T. Kirchner, K. A. Padmanabhan and G. R. Desiraju, *Chem. Commun.*, 2005, 3945–3947.
123 M. S. R. N. Kiran, S. Varughese, C. M. Reddy, U. Ramamurty and G. R. Desiraju, *Cryst. Growth Des.*, 2010, **10**, 4650–4655.
124 M. C. Johnson, J. L. Wang, Z. J. Li, C. A. Lew and Y. S. Yan, *Mater. Sci. Eng., A*, 2007, **456**, 58–63.
125 L. Brabec, P. Bohac, M. Stranyanek, R. Ctvrtlik and M. Kocirik, *Microporous Mesoporous Mater.*, 2006, **94**, 226–233.
126 Z. A. D. Lethbridge, R. I. Walton, A. Bosak and M. Krisch, *Chem. Phys. Lett.*, 2009, **471**, 286–289.
127 G. D. Gatta, *Eur. J. Mineral.*, 2005, **17**, 411–421.
128 G. D. Gatta and Y. Lee, *Phys. Chem. Miner.*, 2006, **32**, 726–732.
129 G. D. Gatta and Y. Lee, *Microporous Mesoporous Mater.*, 2007, **105**, 239–250.
130 S. Ori, S. Quartieri, G. Vezzalini and V. Dmitriev, *Am. Mineral.*, 2008, **93**, 1393–1403.
131 R. M. Hazen and Z. D. Sharp, *Am. Miner.*, 1988, **73**, 1120–1122.
132 R. Arletti, O. Ferro, S. Quartieri, A. Sani, G. Tabacchi and G. Vezzalini, *Am. Miner.*, 2003, **88**, 1416–1422.
133 M. Colligan, P. M. Forster, A. K. Cheetham, Y. Lee, T. Vogt and J. A. Hriljac, *J. Am. Chem. Soc.*, 2004, **126**, 12015–12022.
134 Y. Lee, J. A. Hriljac, T. Vogt, J. B. Parise, M. J. Edmondson, P. A. Anderson, D. R. Corbin and T. Nagai, *J. Am. Chem. Soc.*, 2001, **123**, 8418–8419.
135 P. Comodi, G. D. Gatta and P. F. Zanazzi, *Eur. J. Mineral.*, 2003, **15**, 247–255.
136 P. Comodi, G. D. Gatta and P. F. Zanazzi, *Eur. J. Mineral.*, 2001, **13**, 497–505.
137 G. D. Gatta and Y. Lee, *Microporous Mesoporous Mater.*, 2008, **116**, 51–58.

